



Nonlinear behavior of additively manufactured steel beams with trapped-powder dampers

Jonathan K. Black¹, Brooklyn Andrus¹, Derek Koski¹, Matthew S. Allen *¹, Nathan Crane¹, and Tracy Nelson²

Abstract

Additive manufacturing has gained popularity for its ability to produce complicated geometries that distribute material optimally and allow several parts to be consolidated into one. Part consolidation often comes with a large reduction in damping, however, due to the elimination of frictional losses at interfaces between parts. This reduction of damping can be problematic in applications where resonant vibrations lead to early fatigue failure or undesirable noise emission. In recent years, a promising technique for increasing damping in parts made by laser powder bed fusion (LPBF) has been introduced, in which pockets of retained, unfused metal powder act as embedded dampers. This work presents an experimental study of the nonlinear behavior of several 316L stainless steel rectangular beams made by LPBF with embedded powder dampers. In addition to amplitude-dependent nonlinearity, a significant memory effect is observed, thought to be caused by powder settling and unsettling in response to external agitation. A procedure was developed to measure the full range of damping behavior by causing the system to transition between high-damping and low-damping states. This procedure is applied to six beams with varying pocket thicknesses, resulting in a rich dataset that provides insight into the factors that most influence the effective modal damping and natural frequency of these parts. As pocket thickness increases, the damping increases, together with the amount of nonlinearity and the variance in damping and natural frequency. This uncertainty can be reduced by controlling the amplitude range of interest, the powder state, the drive point, the impact force, and the hammer tip. The relative importance of each of these factors is quantified, and each factor is found to be significant in certain cases. Some of the parts are shown to exhibit significant modal interactions, as well as time-varying phenomena, for some modes. Additionally, a study which varied the operating temperature is presented, confirming that the behavior of trapped-powder dampers is largely temperature-independent. Implications of these findings for design and modeling are discussed.

Keywords: Damping; Additive Manufacturing; System Identification; LPBF; Particle Damper

Received on March 13, 2025, Accepted on October 7, 2025, Published on October 9, 2025

1 Introduction

Additive manufacturing (AM) allows designers to create complicated geometries that would traditionally be manufactured as assemblies of several simpler parts. While part consolidation can have many advantages [1], it generally leads to a large reduction in damping because friction at interfaces between parts tends to be the primary source of damping in an assembly [2]. Structures with low damping have high response amplitudes at resonance, which can

*matt.allen@byu.edu

¹ Brigham Young University, (Department of Mechanical Engineering), Provo, UT 84602, USA

² Brigham Young University, (Department of Manufacturing Engineering), Provo, UT 84602, USA

lead to early fatigue failure [3] or increased noise emission. Reintroducing damping in these cases would be very desirable

Viscoelastic damping treatments, in which layers of rubber or some other viscoelastic material are adhered to a part, dissipate mechanical energy through the hysteretic material damping of the viscoelastic. Though commonly employed, these treatments are most effective in a narrow temperature range because viscoelastic material properties are highly temperature-dependant [4]. Furthermore, the adhesives used to bond viscoelastics to a surface have limited stiffness and strength. These factors make viscoelastic treatments less appropriate for applications where the part is exposed to high temperatures or large accelerations. Particle impact dampers have been studied for use in these more extreme applications [5, 6, 7, 8], and their potential costs, benefits and complexities are highlighted in those works and in a recent review [9]. Particle dampers can be assembled and mounted on the structure to be damped, or they can be embedded by machining a cavity in the structure, filling it with particles, and re-sealing it. During vibration, the trapped particles dissipate energy, primarily by inelastic impacts and frictional losses, contributing to significant increases in modal damping.

Particle dampers can be embedded in parts made by laser powder bed fusion (LPBF) without the need for any post-processing by leaving cavities filled with unfused feedstock powder. While traditional particle dampers generally use particles between $50\,\mu m$ and $5\,m m$ [8] in diameter, this technique uses feedstock powder, which often has mean particle diameters less than $50\,\mu m$. This difference in particle diameter leads to significantly different rheological behavior. To emphasize this distinction, the present work uses the term "trapped-powder damper" for particle dampers utilizing fine powders, like AM feedstock, for the particles. Early studies of AM trapped-powder dampers [10, 11] saw near order of magnitude decreases in response at resonance (i.e. increases in damping) with the addition of thin pockets of trapped powder. In recent years, a few groups have begun to study the effect of varying placement, geometry, and orientation of these LPBF powder dampers [12, 13, 14].

Although several studies have reported significant amplitude-dependent nonlinearity in the damping behavior of AM trapped-powder dampers, this nonlinearity is still not very well understood. Künneke and Zimmer [10] performed free vibration measurements on AM parts with embedded powder dampers, and the logarithmic decrement was found to decrease by nearly an order of magnitude over the course of the ring-down. Guo et al. [13] studied the forced response of AM trapped-powder dampers, and they found the loss factor to vary significantly with both excitation frequency and amplitude. Westbeld et al. [15] performed forced vibration tests on powder-damped LPBF beams, and they similarly found the loss factor to depend on the excitation amplitude, and the magnitude of that effect depended on the mode being excited. Shu et al. [16] performed system identification to characterize the amplitude-dependent nonlinearity of a bolted assembly of AM parts with trapped-powder dampers. While their treatment of the nonlinearity was more rigorous than other studies, the presence of the bolted joint in this system makes it difficult to disambiguate the effect of the trapped powder from that of the bolted joint nonlinearity. Much work has been done to understand the nonlinear behavior of traditional particle dampers [9], which generally have particle diameters in the millimeter range, but recent work by Kiracofe et al. [17] suggested that trapped-powder dampers behave differently from traditional particle dampers because cohesive forces are relevant due to the small diameter of the feedstock powder particles. This conclusion aligns well with the observation that trapped AM feedstock powder does not flow freely within a cavity when the part is reoriented [12, 15]. The nonlinear behavior of AM parts with trapped-powder dampers merits further study.

Even when accounting for amplitude-dependent nonlinearity, significant variability has been seen in the damping of these parts. This variability, if left unexplained, could prove an obstacle to the application of this technology. In a case study of an AM brake disk with trapped powder, Künneke and Zimmer [10] reported significant reductions in sound intensity compared to a conventionally manufactured disk, but the AM disk had more than twice as much variability in the measured sound intensity. They hypothesized that powder solidification may explain some of that variability. Scott-Emuakpor et al. [18] performed high-strain fatigue testing on components with pockets of trapped powder and observed a decrease in damping over the course of the experiment as the powder fused to the walls of the cavity. Westbeld et al. [15] performed forced vibration tests on powder-damped LPBF beams and reported that the modal damping decreased significantly over the course of the experiment for some modes. CT scanning revealed that this decrease in damping over time was accompanied by powder settling.

Our recent studies of LPBF beams with trapped-powder dampers have begun to explain the sources of this variability. In addition to amplitude-dependence, we observed a reversible memory effect: certain kinds of external agitation were found to cause the system to transition between a high-damping state and a low-damping state [19]. The authors studied this memory effect carefully for the first bending mode of a single beam in [19], and the results suggested that it was caused by powder settling and unsettling.

The goal of the present work is to provide an experimental database that thoroughly elucidates the effect of trapped powder on the nonlinear response of beams with trapped-powder dampers. The present work extends that

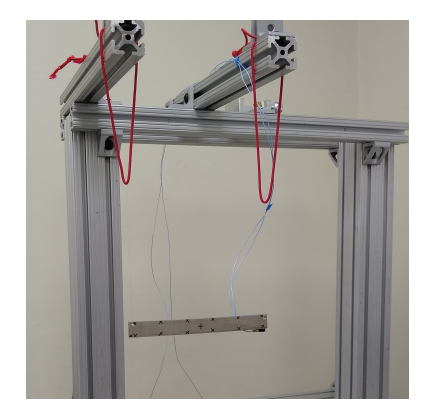
in [19] by studying six beams, each one having a trapped powder pocket of a different thickness. Furthermore, several modes of vibration are studied, including bending in two directions and torsion, to see how the frequency and damping of each mode are affected by the pocket of trapped powder. The present study varied the vibration amplitude, powder state, and impact force and location, shedding further light on the effect of each of these factors on the damping and natural frequency of each mode. Significant modal interactions are observed for some of the beams and these are discussed. Additionally, one beam was tested at several temperatures to see if the operating temperature had any discernible effect on the damping (see Section D). The results presented here provide a rich database for those seeking to model the effects of trapped powder on the damping of additively manufactured parts.

2 Methods

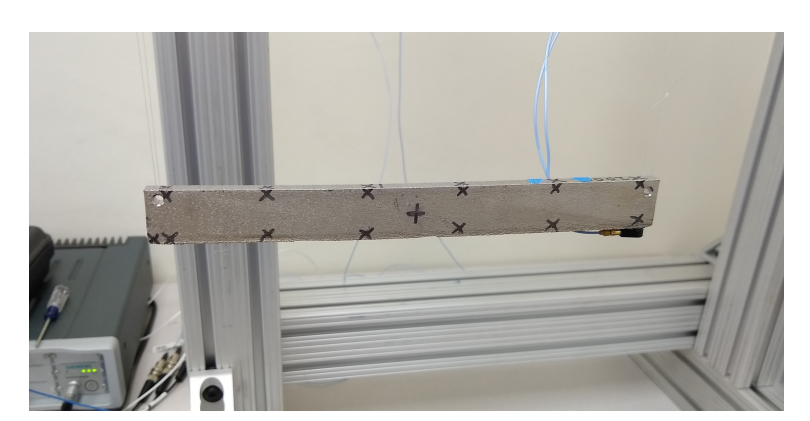
As detailed by Teng [20], various rectangular beams were manufactured by LPBF on a Concept Laser M2 Cusing. The feedstock was 316L stainless steel powder (GE CL 20ES) with a mean particle size of $29.9\,\mu\mathrm{m}$ ($15-45\,\mu\mathrm{m}$). The beams were not subjected to any kind of heat treatment. Each of the beams had the same major dimensions, nominally $(180\times18\times6)\mathrm{mm}$, while the dimensions of a pocket of trapped, unfused powder were varied between the samples. The beams tested in the present work had nominal pocket dimensions of $140\,\mathrm{mm}\times16\,\mathrm{mm}\times H_p$, with $H_p\in\{0,100,500,1000,2000,3000\}\mu\mathrm{m}$. (Pocket thickness $H_p=0$ refers to a fully-fused beam.) The measured mass and dimensions of the beams are tabulated in section B, together with a labeled drawing.

2.1 Experimental setup

Holes drilled in the top corners of the beams facilitated hanging them from fishing line, which was then suspended from bungee cables, as shown in Fig. 1. This low-stiffness support system approximates free-free boundary conditions and minimizes the energy lost in the form of waves traveling along the supports. Two PCB 352C22 accelerometers were glued near the corner of the beam with Loctite Super Glue. The accelerometer wires were taped near a node line of Mode 1 to minimize the added damping due to the wiring. Fig. 2 explains the coordinate system and abbreviations that will be used to refer to points on the beams at which impacts were applied with instrumented hammers.



(a) Suspension system.



(b) Close-up on the beam. Compare with Fig. 2.

Fig. 1: Photos of the experimental setup.

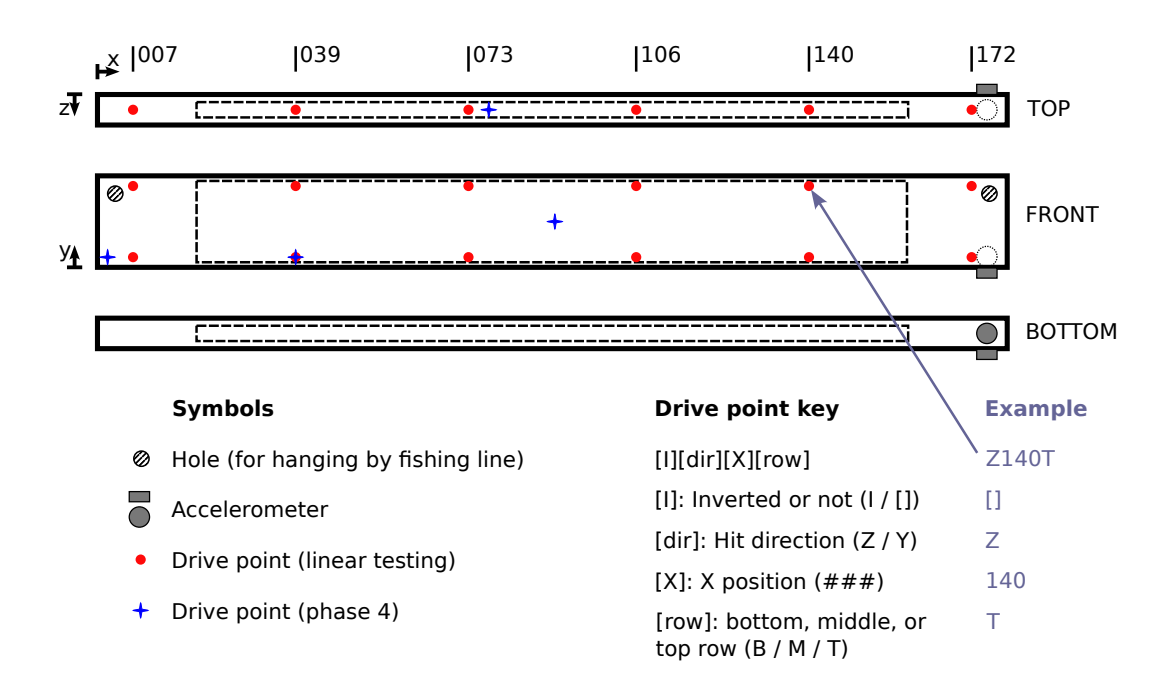


Fig. 2: Diagram of beam, showing hit locations. The "Drive point key" explains the abbreviations that will be used to refer to points on the beam. The *X* position coordinates are given in millimeters.

2.2 Nonlinear system identification

As we have previously observed significant nonlinearity in these parts, we collect acceleration time histories and identify nonlinear system parameters by a variation on Feldman's FREEVIB method [21]. The system identification method decomposes the measured free response into a sum of damped oscillations, each of which is assumed to have the following form:

$$q(t) = \operatorname{Re}\left\{A_0 \exp\left(-\beta(t)\right) \exp\left(i\phi(t)\right)\right\} \tag{1}$$

where $\text{Re} \{\cdot\}$ denotes the real part, $A_0 \exp(-\beta(t))$ is the decay envelope with potentially time-varying decay rate, and $\phi(t)$ is the phase angle. While acceleration measurements are used in the present study, the method can be applied to free ring-down measurements of position, velocity, or acceleration.

First, the measured signal must be decomposed into unimodal ring-downs. This is done with digital Butterworth band-pass filters in the present work, as illustrated in fig. 3. Next, the complex, analytic signal representation of the measured signal is constructed as follows:

$$Q(t) = q(t) + i\tilde{q}(t) \tag{2}$$

where $\tilde{q}(t)$ is the Hilbert transform of the measured signal q(t). This analytic signal Q(t) can then be used to identify the parameters in eq. (1) as follows:

$$\angle Q(t) = \phi(t)$$
 (3)

$$\ln(|Q(t)|) = \ln(A_0) - \beta(t) \tag{4}$$

where $\angle Q$ and |Q| represent the argument and modulus of Q, respectively, and $\ln(\cdot)$ is the natural logarithm.

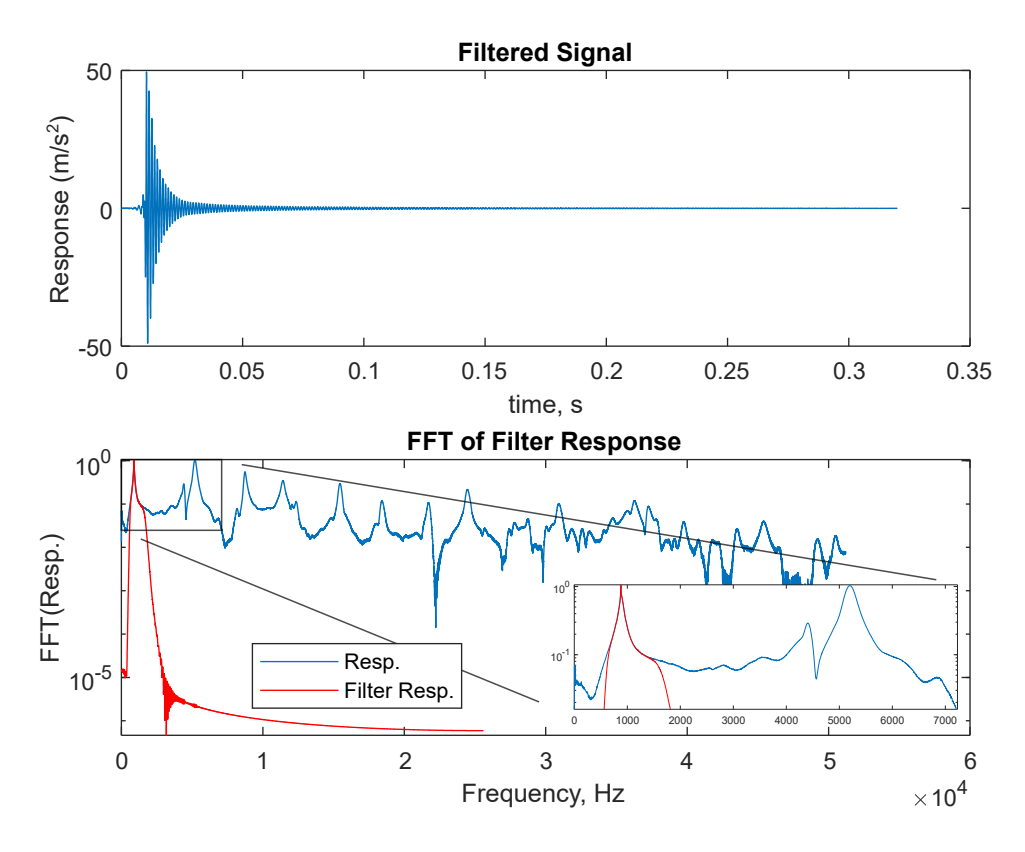


Fig. 3: Band-pass filtered acceleration signal for an example ring-down measurement. The Fast Fourier transform (FFT) of the acceleration is also plotted, along with the FFT of the band-pass filtered response.

Next, time-varying parameters $\omega_n(t)$ and $\zeta(t)$ are defined and identified in analogy to the natural frequency and damping ratio of a linear system. For a linear time-invariant system, the damped natural frequency is the rate of change of the phase angle, so $\phi(t) = \omega_d t$. For a nonlinear system, the instantaneous frequency $\omega_d(t)$ is defined analogously as follows:

$$\omega_d(t) \triangleq \frac{d\phi(t)}{dt} = \frac{d}{dt} \left(\angle Q(t) \right) \tag{5}$$

The instantaneous natural frequency $\omega_n(t)$ and damping ratio $\zeta(t)$ are then found by the following equations.

$$\alpha(t) \triangleq -\frac{d\beta(t)}{dt} = \frac{d}{dt} \left(\ln\left(|Q(t)| \right) \right) \tag{6}$$

$$\omega_d(t) \triangleq \omega_n(t) \sqrt{1 - \zeta(t)^2} \tag{7}$$

$$\omega_n(t) = \sqrt{\omega_d(t)^2 + (\zeta(t)\omega_n(t))^2} = \sqrt{\omega_d(t)^2 + \alpha(t)^2}$$
(8)

$$\alpha(t) = -\zeta(t)\omega_n(t) \tag{9}$$

$$\zeta(t) = \frac{-\alpha(t)}{\omega_n(t)} \tag{10}$$

The derivatives in eqs. (5) and (6) are prone to accentuating noise in the signal. Our implementation fits $\angle Q(t)$ and $\ln |Q(t)|$ to piecewise linear functions with manually defined endpoints to smooth over noise, as illustrated in fig. 4. The spacing of the endpoints can be chosen to give higher resolution in regions with high signal-to-noise ratio and lower resolution in noisier regions.

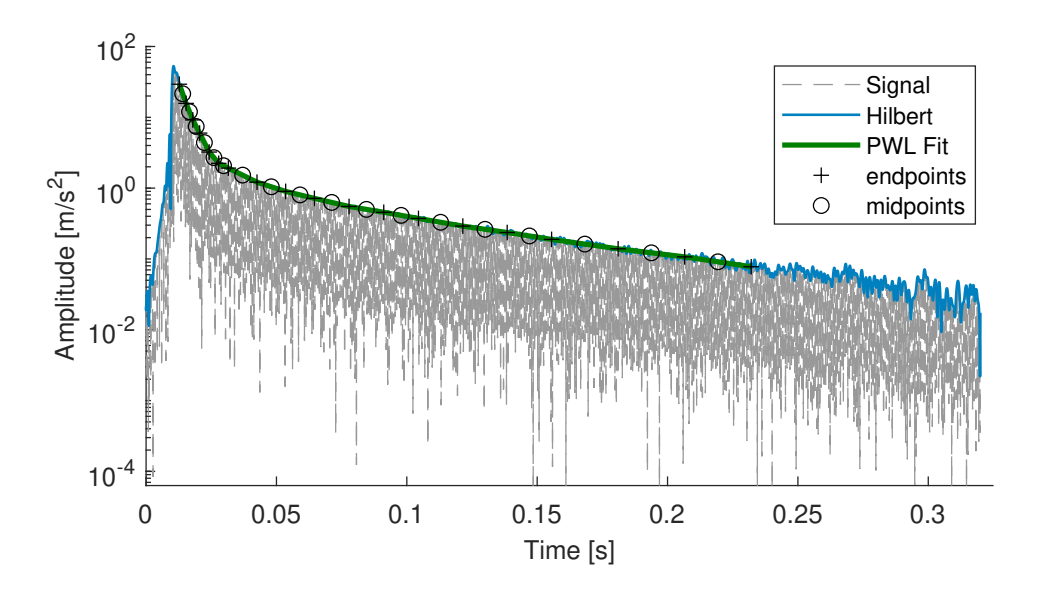


Fig. 4: Piecewise linear fit of the amplitude |Q(t)| of the filtered acceleration signal q(t) from an example ring-down measurement (the same as shown in fig. 3). The line labeled "Signal" is the absolute value of the filtered signal q(t). The line labeled "Hilbert" is the amplitude |Q(t)| of the analytic signal Q(t), and the piecewise linear fit to $\ln |Q(t)|$ is shown in green. The phase $\angle Q(t)$ of the analytic signal is fitted in the same way, though not shown in this figure.

Because many nonlinear systems display amplitude-dependent natural frequency and damping ratio, the quantities $\omega_n(t)$ and $\zeta(t)$ are typically plotted against vibration amplitude $A(t) \triangleq |Q(t)|$. This suggests a correspondence with amplitude-dependent parameters in the quasi-linear system (11). It should be noted, however, that this analogy is only approximate. The response form assumed in eq. (1) does not exactly satisfy equation of motion (11) unless $\omega_n(t)$ and $\zeta(t)$ are constant [22]. If $\omega_n(t)$ and $\zeta(t)$ change slowly, however, then this difference can be neglected.

$$\ddot{q} + 2\zeta(A)\omega_n(A)\dot{q} + \omega_n(A)^2 q = 0 \tag{11}$$

If the response was generated by a system with uncoupled modes, each of which can be described by eq. (11), then repeated measurements should produce the same curves for $\zeta(A)$ and $\omega_n(A)$. Whenever repeated measurements identify significantly different amplitude-dependent system parameters for a given mode, this indicates: 1.) the presence of modal interactions, 2.) that the system is time-varying or 3.) noise or other variability in the measurements. When modal interactions are present, the quantities $\omega_n(A)$ and $\zeta(A)$ in eq. (11) are functions not only of the corresponding modal amplitude A, but also of the amplitudes of other modes as well. The possibility of modal interactions will be discussed in sections 2.4 and 3.3. We have observed time-varying damping and frequency with these beams, which we attribute to powder settling and unsettling, as discussed in Section 2.3. This work addresses that concern by attempting to measure the behavior of the system across the full range of powder states.

2.3 Controlling powder state

An exploratory study confirmed that the system could be made to transition between a high-damping state and a low-damping state by repeatedly tapping the beam. That study focused on Mode 1 of B3000, the beam with a 3 mm powder pocket. The powder in the beam was agitated by tapping the beam at various locations and with various force levels. The methods and results of that study are described in detail in [19], but the most relevant findings are summarized here because they greatly influenced the design of the procedure described in section 2.4.

Tapping the beam from above with relatively small forces proved to be the kind of agitation that led to the largest decreases in damping ratio; an example demonstrating this is included here in fig. 5. Before the measurements

labeled "Y_meas1_hit1" and "Y_meas2_hit1", the beam was struck ten (10) times from above, similar to the "settling hits" depicted in fig. C.1a. Each of the measurements in fig. 5 was obtained by tapping the beam at Z090M (the center of the front face) with an instrumented hammer, and each is labeled "hit1", "hit2" and "hit3". Note that each round of agitation led to a decrease in the damping ratio and an increase in the low-amplitude natural frequency. We attribute this decrease in damping to the powder settling in response to the agitation hits. Also, some additional settling appears to have occurred within each group of three measurements because of the Z-direction impacts used to excite vibrations in the beam.

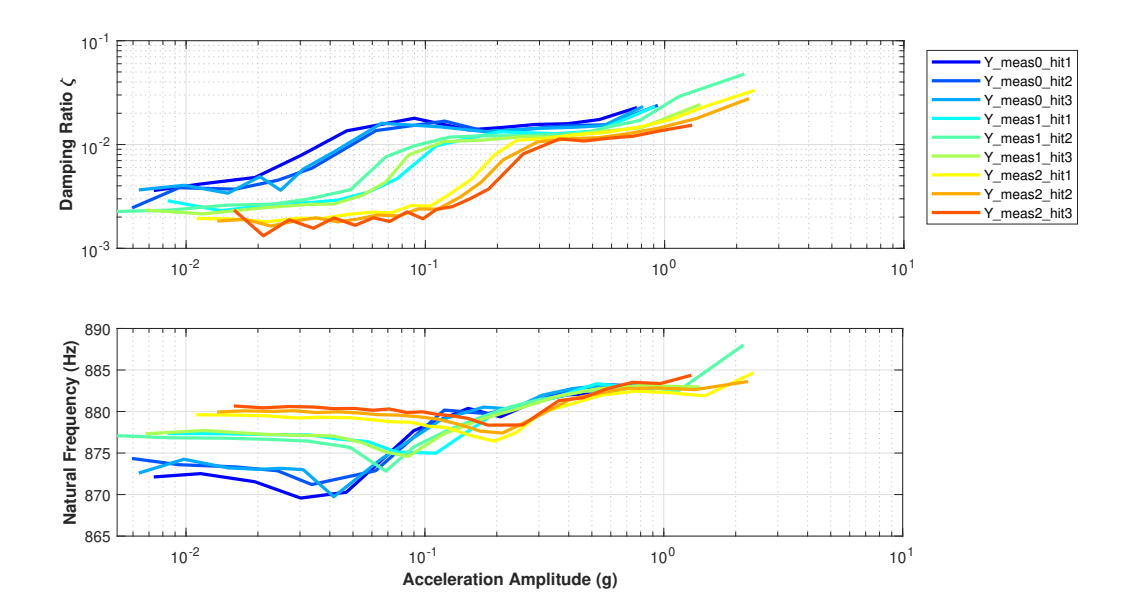


Fig. 5: Damping and natural frequency of Mode 1 versus acceleration amplitude from measurements 0, 1, & 2 of the series of tests for which the beam was agitated by being struck ten times in the Y-direction before each measurement. This was similar to the **settling** procedures used in the present work. For each measurement, the transient vibration was recorded in response to three hits at Z090M, the results of which are shown in the figure. Note the steady progression towards a low-damping, near-constant-frequency state.

The effect of holding the beam upside down in between measurements is shown in Fig. 6. Note that the decreases in damping observed in Fig. 5 are largely reversed by holding the beam upside down. Additionally, it was found that tapping the beam from above while held upside down, as shown in fig. C.1b, led to further increases in damping. (Those results are not shown here, but are discussed in [19].) Thus, we conclude that the decreases in damping observed in Fig. 5 were not the result of an irreversible process like powder fusing to the walls of the cavity or polishing of internal cavity surfaces. Instead, we suggest powder settling and unsettling as the mechanism behind these changes. This explanation agrees with the work of Westbeld et al [15], in which a decrease in damping was correlated with powder settling. Accordingly, in this work we refer to the state reached after repeatedly tapping the beam while hanging normally as the "settled" state (abbreviated "set") and the state reached after tapping the beam while upside-down as the "unsettled" state (abbreviated "uns").

The state of the powder inside the pocket gives the system memory of previous inputs, presenting some challenges for designers hoping to implement this technology. First, it means that, even if amplitude-dependence is controlled for, a single measurement of the damping and natural frequency may be insufficient for understanding the full range of possible system behaviors. In the worst-case scenario, a part could be manufactured and measured to have a high damping ratio which then decreases dramatically over the life of the product due to powder settling, resulting in failure due to resonance. Second, this memory effect means that erroneous conclusions could be drawn when comparing several parts with particle dampers. For example, if two versions of a design incorporating a trapped powder pocket are manufactured, but the powder state is not carefully controlled for when testing them, then one could draw erroneous conclusions regarding which design provides better performance.

The approach taken in the present work to account for this memory effect is to attempt to observe the upper and lower bounds of possible system behaviors for each part studied. This is done by intentionally driving the system to the most settled and unsettled states and measuring the damping and natural frequency at each extreme. Although the state of the powder is not fully characterized by a binary classification as "settled" or "unsettled", this approach

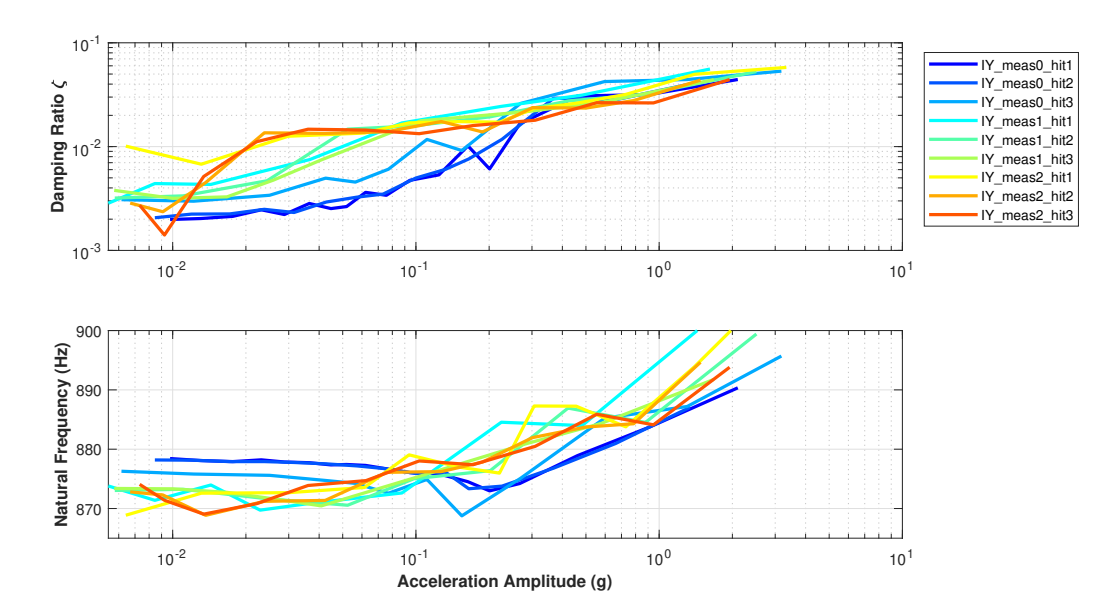


Fig. 6: Damping and natural frequency curves for Mode 1 from the series of tests for which the beam was held in an inverted position for one second before "IY_meas1_hit1" and five seconds before "IY_meas2_hit1". This had a similar effect as the **unsettling** procedures used in the present work, although in the present work the beams were also tapped lightly from above while inverted, which further promoted unsettling. Note that the low-amplitude damping increased and the low-amplitude natural frequency decreased, the opposite of the changes seen in Fig. 5

should allow us to identify the upper and lower bounds on the damping ratio and natural frequency and give us some understanding of how much the system behavior is affected by the powder state.

2.4 Bounding system behavior

The four-phase procedure summarized in Table 1 seeks to quantify the dependence of modal frequency and damping on amplitude and powder state for a given part. The second phase determines whether powder settling and unsettling has a significant effect on any mode, and when it is found to have a significant effect the third phase adjusts the settling and unsettling procedures to ensure that the full range of settled and unsettled states are observed. Finally, measurements are acquired for all modes of interest.

Table 1: Summary of four-phase procedure for characterizing modal frequency and damping for a given part.

Phase	Description	Output
1	Linear EMA (low-amplitude)	Natural frequencies and mode shapes
2	Memory effect detection	Which mode, if any, is most affected by powder state
3	Optimize powder settling and unsettling	Procedures for repeatable settling and unsettling
4	Measure all modes in every powder state	Amplitude-dependent frequency and damping for all modes

Phase 1 consists of standard, linear experimental modal analysis (EMA) to identify natural frequencies and mode shapes of the modes of interest. The hammer used was a PCB 084A14 with PCB 086E80. Very low force amplitudes (mostly 1-5 N) are used in this phase to avoid exciting the amplitude-dependent nonlinearity. The natural frequencies identified in this phase will later be used to determine the frequency range over which to band-pass filter the measurements for nonlinear system identification (see section 2.2).

Phase 2 seeks to determine whether powder state has a significant effect on the (amplitude-dependent) damping and frequency of any mode, and which mode is most strongly affected. This is done by performing two consecutive rounds of settling, followed by two rounds of unsettling, followed by two more rounds of settling. The frequency and

damping of each mode are measured after each round of settling or unsettling. The details of the procedure for Phase 2 are given in Appendix C.

If no significant memory effect is observed in Phase 2, then we skip to an abbreviated version of Phase 4, in which all modes of interest are measured, but no attempt is made to control the powder state. This abbreviated procedure is significantly less labor intensive, so it is desirable to identify cases where the powder state has a negligible effect.

If, however, Phase 2 determines that the powder state has a significant effect, then Phase 3 is performed to determine suitable settling and unsettling procedures for the given beam. The number of hits, location of hits, and force levels used for agitation are variables which Phase 3 seeks to optimize by iteration, with the goal of maximizing the difference between the "settled" and "unsettled" states. This should make it possible to measure the upper and lower bounds on damping and natural frequency. The procedure for Phase 3 is discussed in more detail in section C.

While there is no guarantee that the settling and unsettling procedures will produce the most settled and unsettled states possible or that the powder will be in exactly the same state every time one of these procedures is run, performing Phase 3 can develop procedures that approach those two ideals. In any case, the measurements in Phase 4 are all repeated several times, ensuring that a wide array of data is collected and allowing the repeatability of the measurements to be quantified.

Once the settling and unsettling procedures are determined to be appropriate—capable of causing the powder to transition between fully settled and fully unsettled states—Phase 4 can be executed. The goal of Phase 4 is to measure the upper and lower bounds of the amplitude-dependent damping and natural frequency for each mode in the frequency range of interest. This is done by intentionally driving the system between the settled and unsettled states, using the procedures developed in Phase 3, and then exciting the beam at multiple points so that all modes of interest are measured. Each combination of powder state, hammer type, and drive point is measured four times, with the order being randomized, to provide statistical confidence in the results.

Four drive points were chosen, each of which excites different modes. See Fig. 2 for a diagram showing the location of those four points and the key to hit location abbreviations. Since it is known that measurement hits can affect the powder state, we randomize the hit order between the four drive points. While it would have been possible to excite all modes of interest with just two drive points (Z002B and Y077), the additional two drive points (Z039B and Z090M) will enable the detection of modal coupling. Z039B was chosen to be at the node of the first soft direction bending mode, so it excites all torsion modes and all soft direction bending modes besides the first one. Z090M excites only the odd-numbered soft direction bending modes. For each mode that is excited by two or more of the three Z-direction drive points, we will be able to detect whether its apparent damping and frequency are affected by the presence of other modes, which would indicate the presence of modal interactions.

Comparing measurements taken with two different hammers will also facilitate the detection of modal coupling. The medium hammer (PCB 086C01) is equipped with a plastic tip, so it will impart more energy to the lower frequency modes than the small hammer (PCB 084A14 with PCB 086E80), which has a metal tip. Varying the hit force and hammer tip, therefore, provides another way to change the extent to which the various modes are excited.

After processing the acceleration signals as described in Section 2.2, the identified natural frequency and damping can be plotted as functions of amplitude. Inspecting these plots allows conclusions to be drawn about the ranges of damping and frequency that can be expected for a given mode and how those values depend on various factors.

3 Results and discussion

The four-phase procedure described in Section 2.4 was carried out for six beams, resulting in a rich set of nonlinear damping and frequency measurements. Section 3.1 presents results for a single beam in order to demonstrate the typical behavior of the nonlinearity for all modes of interest, and Section 3.2 summarizes the results for all beams. Sections 3.3 and 3.4 discuss and quantify the contributions of amplitude-dependence, powder state, and modal interactions to the total variability.

In this section, abbreviations are used to refer to the various modes of interest. The soft direction bending modes are abbreviated "Mode Z#", and the stiff direction bending modes are abbreviated "Mode Y#", in reference to the direction of motion and the coordinate system in Figure 2. The torsional modes are abbreviated "Mode T#". Hence, the first mode, mentioned in Figures 5 and 6, will be denoted "Mode Z1" from this point forward.

3.1 Results for one beam

This section will present results for B1000, the beam with a 1 mm powder pocket. The naming convention for the beams is that the number following the letter "B" refers to the thickness of the powder pocket in microns.

Figures 7 to 9 show the mode shapes and natural frequencies found in Phase 1 for the first few modes of each kind. The modes in the Y- and Z-directions were processed independently, using only the relevant drive points and accelerometer. Each mode shape is very similar to the corresponding analytical mode shape expected for a free-free Euler-Bernoulli beam. Some deviation is expected, in part because the stiffness and density of the beam vary with position due to the powder pocket, but the mode shapes of every beam tested were found to be qualitatively very similar to these.

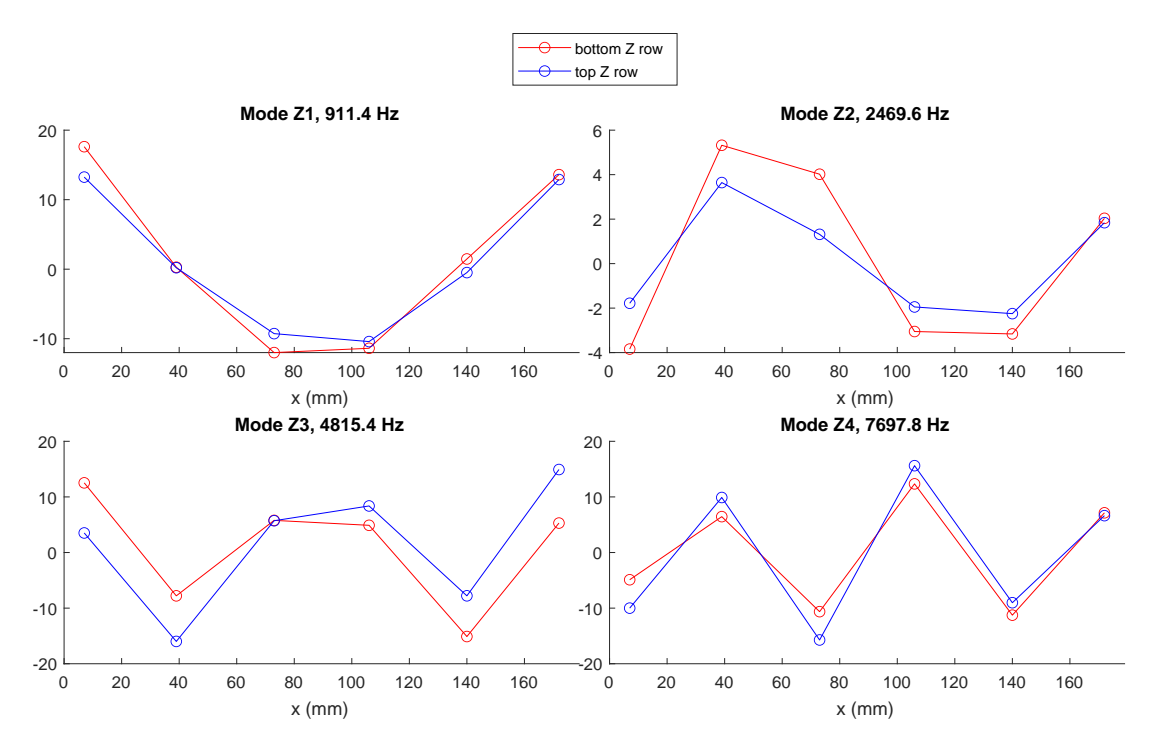


Fig. 7: Experimentally measured mode shapes for the first 4 soft direction bending modes of B1000. The scaling is arbitrary.

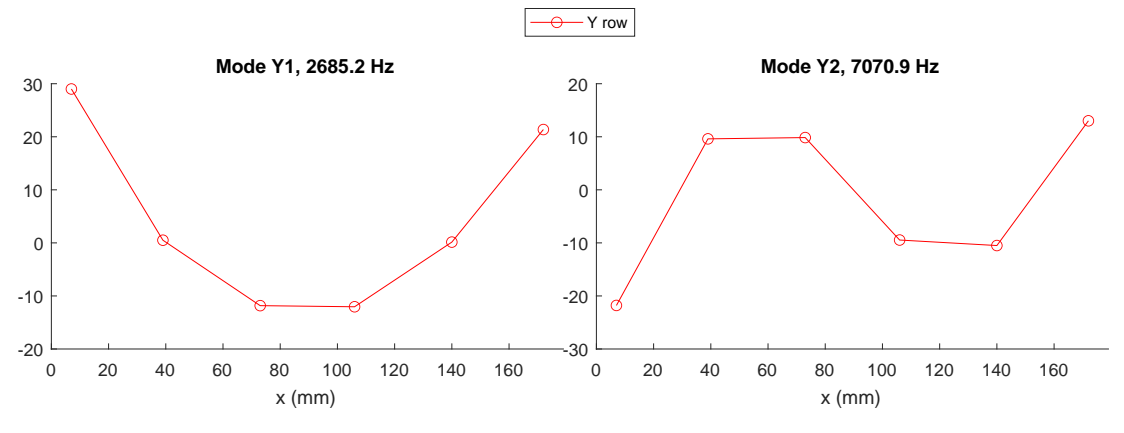


Fig. 8: Experimentally measured mode shapes for the first 2 stiff direction bending modes of B1000. The scaling is arbitrary.

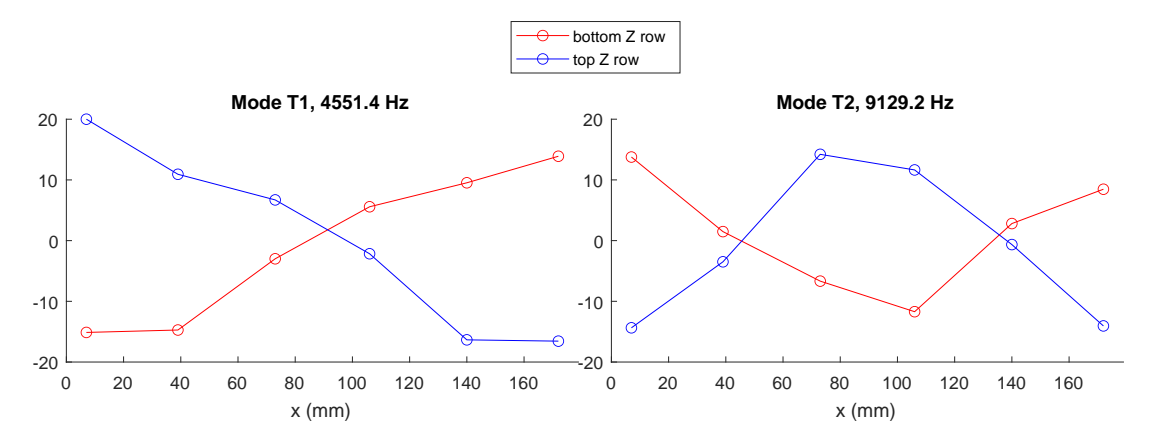


Fig. 9: Experimentally measured mode shapes for the first 2 torsion modes of B1000. The scaling is arbitrary.

Figure 10 shows the identified damping and frequency curves from Phase 4 for the first two soft direction bending modes (Modes Z1 and Z2). The acceleration amplitude on the abscissa of these plots is in physical, not modal coordinates. It corresponds to the acceleration measured at the corner of the beam, after band-pass filtering so that only the mode in question remains in the response. See Fig. 2 for the location of the accelerometers. The colors of the lines distinguish the individual measurements. The legends were omitted in these plots, but the details regarding the drive point and powder state etc. for each measurement are available in the supplementary files. The damping and natural frequency clearly depend on vibration amplitude: both generally increase with amplitude. However, the high variability between measurements suggests that amplitude is not the only relevant variable, as will be discussed further in Section 3.3.

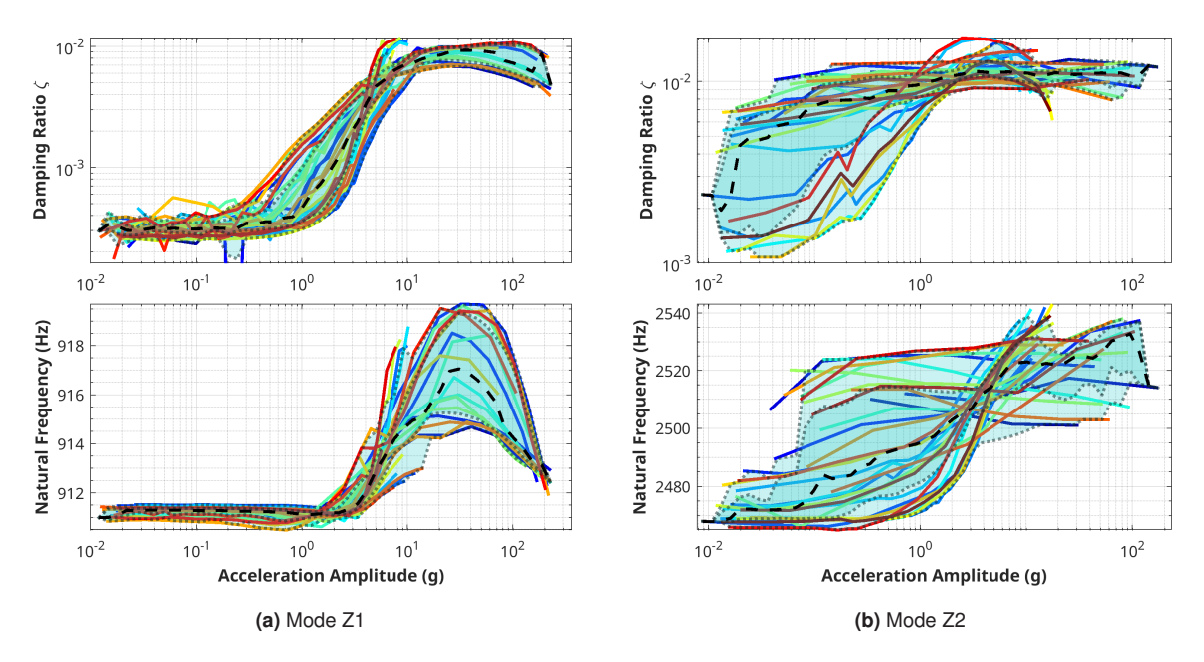


Fig. 10: Damping ratio and natural frequency for the first two soft direction bending modes of B1000. The dashed black line is the median, and the transparent turquoise envelopes show the interquartile range and the full range, excluding outliers. As in a traditional box and whisker chart, points are considered outliers if they fall more than $1.5 \times IQR$ above the third quartile (q_3) or below the first quartile (q_1) , where IQR is the interquartile range $(q_3 - q_1)$.

Fig. 11 presents the results for Modes Z3 and Z4. In contrast to the first two, the damping of these modes decreases with amplitude, while the frequency increases with amplitude. These modes also show smaller changes in damping with amplitude, both decreasing by a factor of one-third to one-sixth of their peak damping values. In contrast, the damping of Modes Z1 and Z2 increased by an order of magnitude. Note that these graphs do not include measurements taken with the medium hammer, as it did not excite these higher-frequency modes well enough for them to be separated from noise and the influence of nearby modes by band-pass filtering.

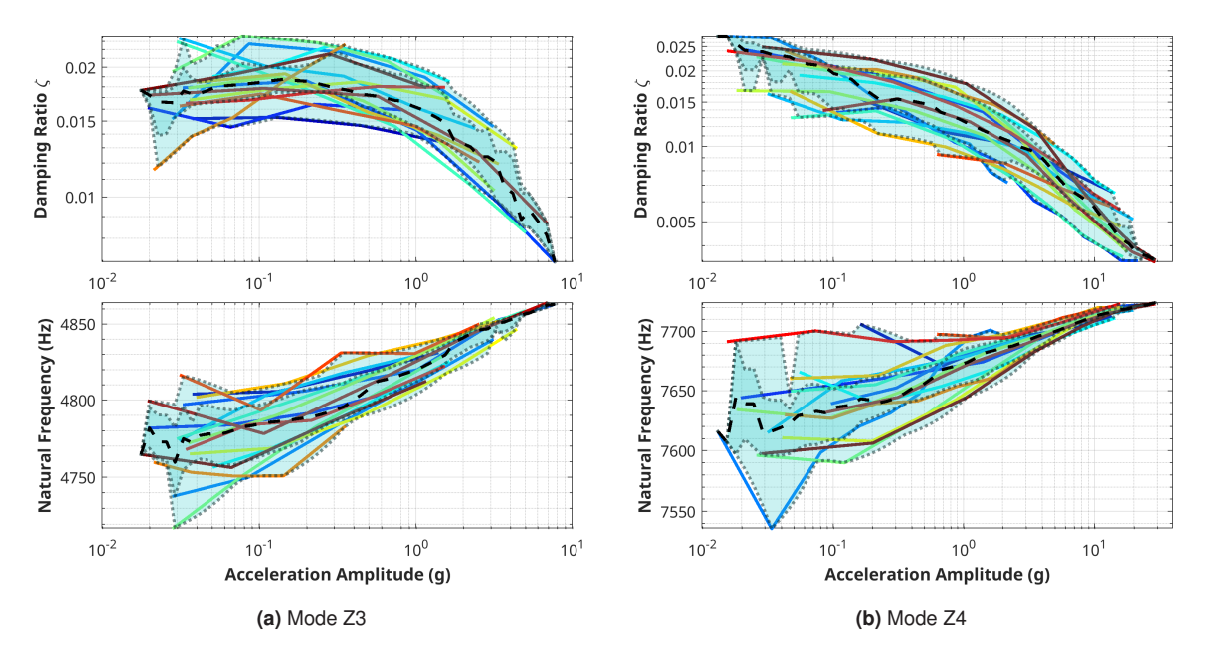


Fig. 11: Damping ratio and natural frequency for Modes Z3 and Z4 of B1000. The dashed black line and the transparent envelopes are interpreted as in Figure 10.

The results for the stiff direction bending modes are plotted in Fig. 12. The damping for Mode Y1 increases by more than an order of magnitude and then decreases by a similar amount. This contrasts the behavior of the first four soft direction modes in Figs. 10-11, which either increased or decreased. Few trends can be identified in Mode Y2, due to high variability between trials, although the damping and frequency appear to decrease at high amplitude, and the variability in both becomes small at high amplitudes.

Mode Y1 also exhibits an interesting dip in damping near the high end of the amplitude range, and while the shape of this dip is consistent, it does not occur at a consistent amplitude between measurements. Rather, the dip seems to come shortly below the maximum amplitude of each measurement, suggesting that the damping is a function of time since the impact, and hence that the powder properties are changing with time. The magnitude of this effect is relatively small, however, so it could likely be treated as noise in practice.

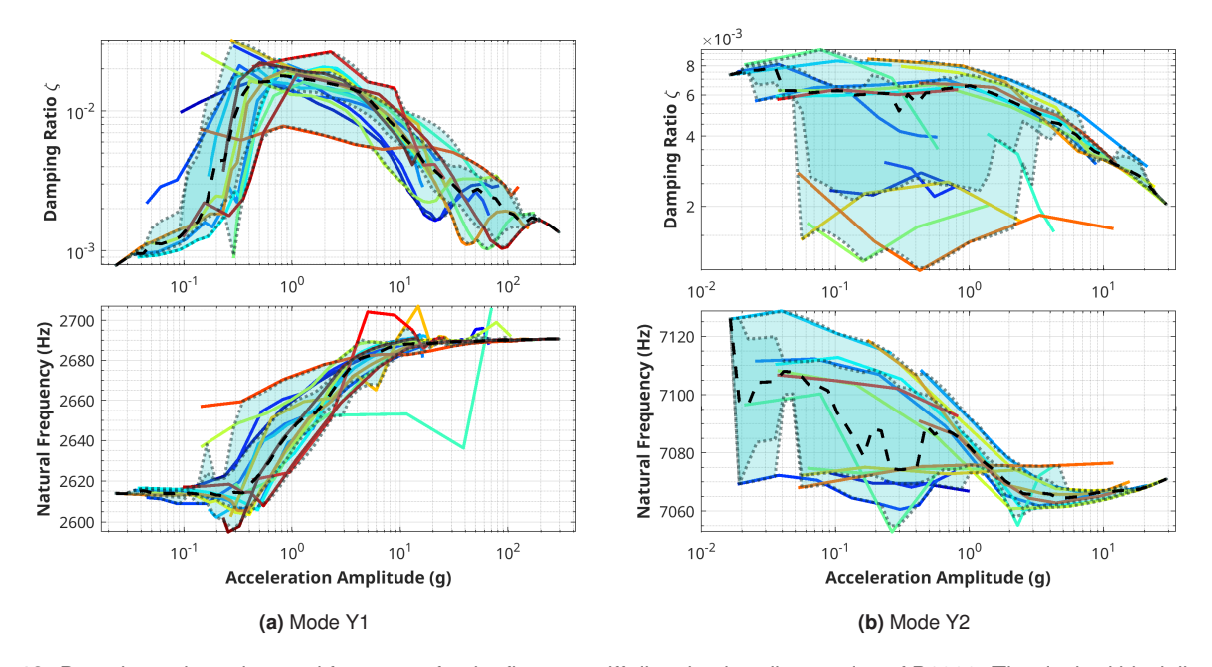


Fig. 12: Damping ratio and natural frequency for the first two stiff direction bending modes of B1000. The dashed black line and the transparent envelopes are interpreted as in Figure 10.

The results for the torsional modes are presented in Fig. 13. Both torsional modes increase in frequency with amplitude. Mode T1 appears to be nearly linear in damping, albeit with considerable variability, while the damping of Mode T2 decreases with amplitude.

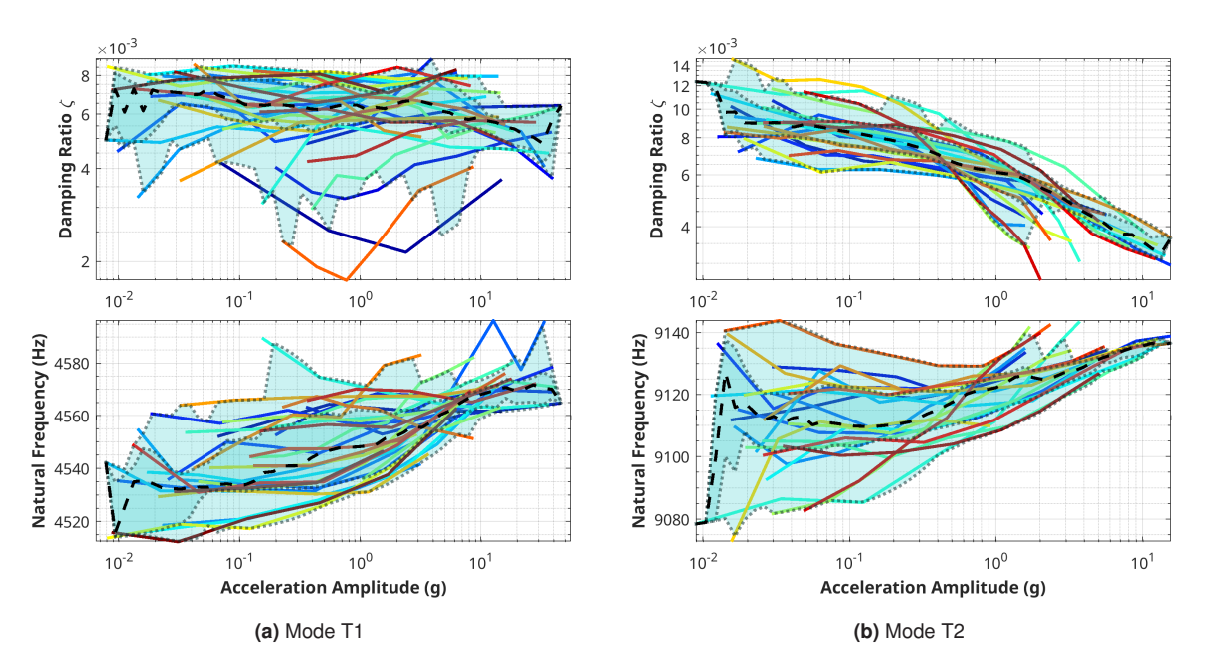


Fig. 13: Damping ratio and natural frequency for the first two torsional modes of B1000. The dashed black line and the transparent envelopes are interpreted as in Figure 10.

Plots like these for every beam and mode considered, along with the data used to make them, are available in the supplementary files.

3.2 Summarized results for all beams

Instead of amplitude-dependence plots for each mode for all six beams tested, summary box plots are given in Figures 14 to 18. The colored boxes show the median and interquartile range. The whiskers show the full range, excluding outliers, which are plotted as colored dots. Points are considered outliers if they fall more than $1.5 \times IQR$ above the third quartile (q_3) or below the first quartile (q_1) , where IQR is the interquartile range $(q_3 - q_1)$.

For each beam and mode, box plots are generated for three amplitude ranges, labeled "low", "all", and "high". The range labeled "all" was chosen to be as large as possible while ensuring that there would be data everywhere in that range for every beam measured. The "low" and "high" ranges were taken to be the lower and upper quarters, respectively, of the full amplitude range. Those quarters are measured in log space, so for example, if the full amplitude range measured for a mode was 10^{-2} g to 10^2 g, the "low" quarter of the data would be the range from 10^{-2} g to 10^{-1} g. It should be noted that there are generally fewer points in the high amplitude range because the hits varied in force, and soft hits generate data only in the lower half of the amplitude range, whereas hard hits generate data in the entire amplitude range. This means that the statistics for the full amplitude range ("all") tend to be skewed towards the low-amplitude behavior.

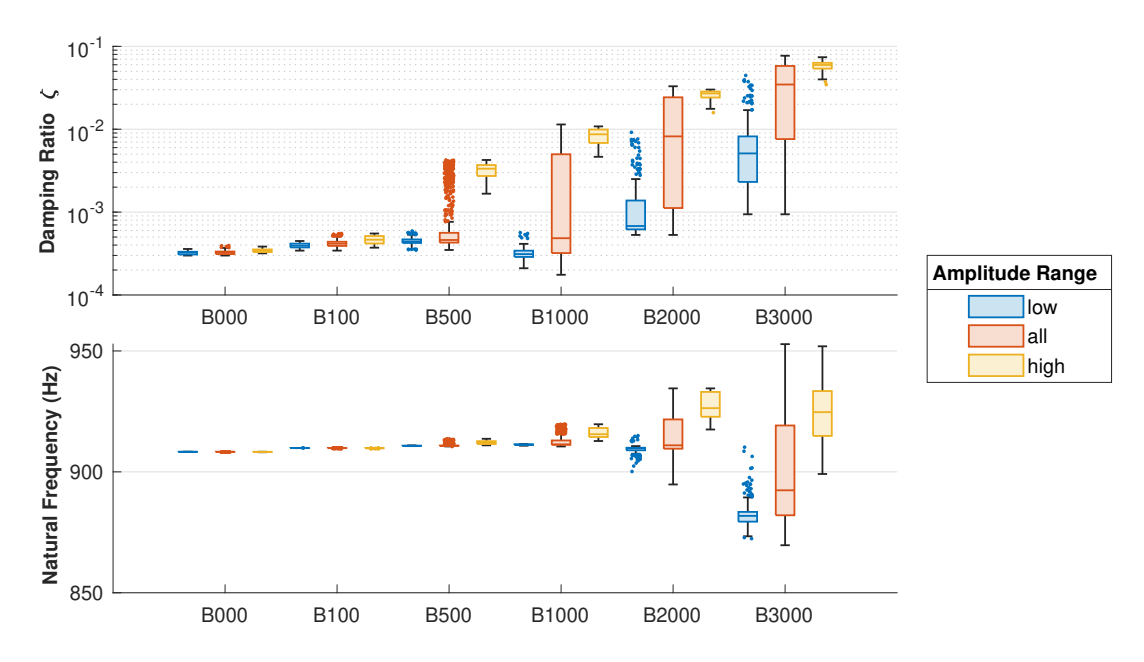


Fig. 14: Summary statistics for damping and natural frequency: Mode Z1. The full amplitude range for this mode is $A \in [1.5 \times 10^{-2}, 2 \times 10^{2}]g$

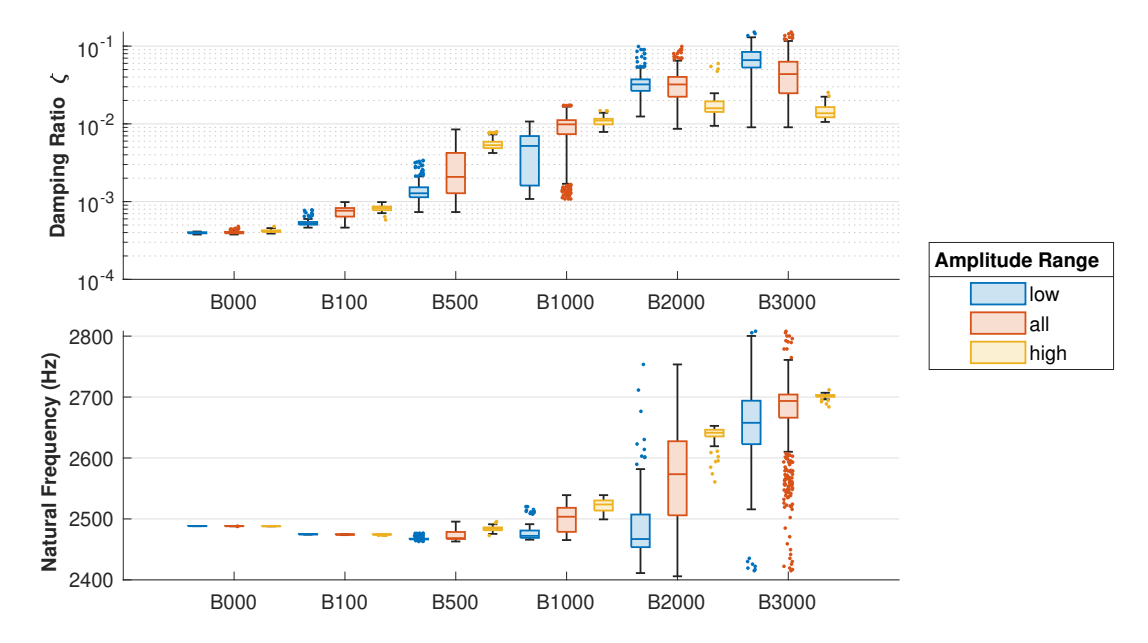


Fig. 15: Summary statistics for damping and natural frequency: Mode Z2. The full amplitude range for this mode is $A \in [8.8 \times 10^{-3}, 8.93 \times 10^{1}]g$

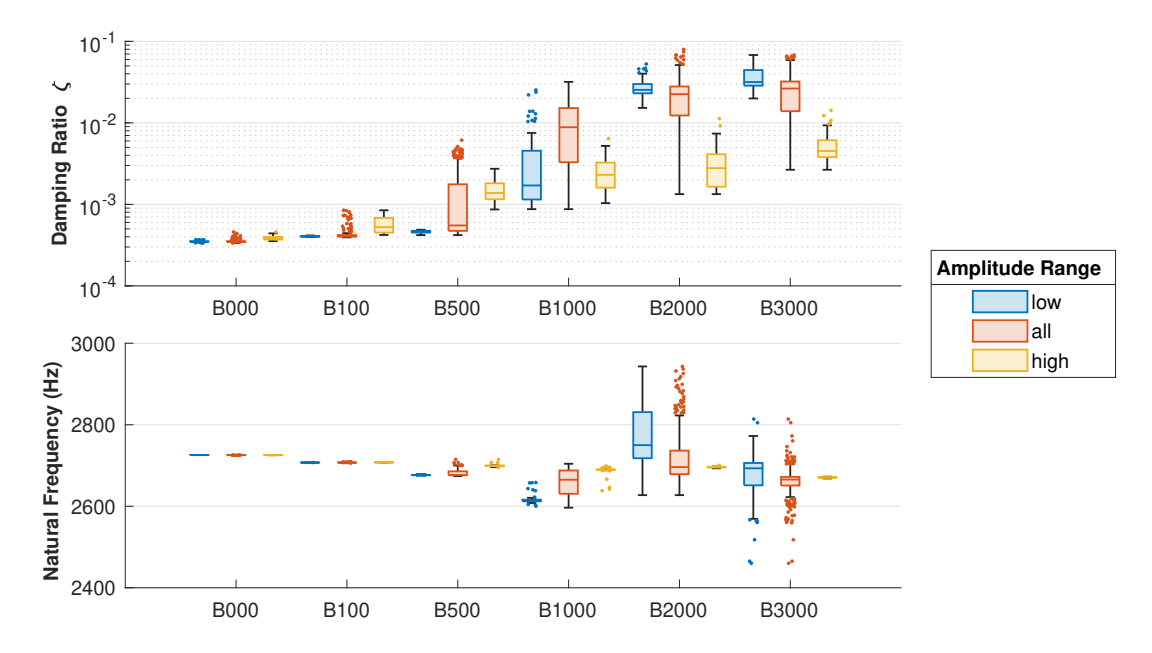


Fig. 16: Summary statistics for damping and natural frequency: Mode Y1. The full amplitude range for this mode is $A \in [2.83 \times 10^{-2}, 2.47 \times 10^{2}]g$

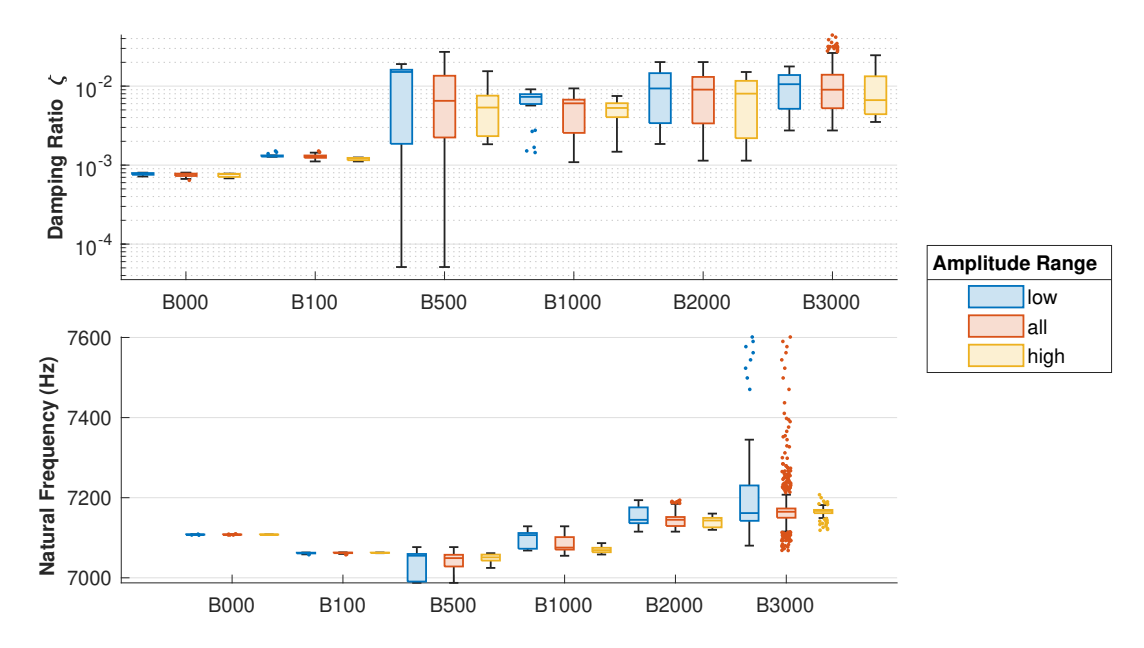


Fig. 17: Summary statistics for damping and natural frequency: Mode Y2. The full amplitude range for this mode is $A \in [1.75 \times 10^{-2}, 4.83 \times 10^{0}]g$

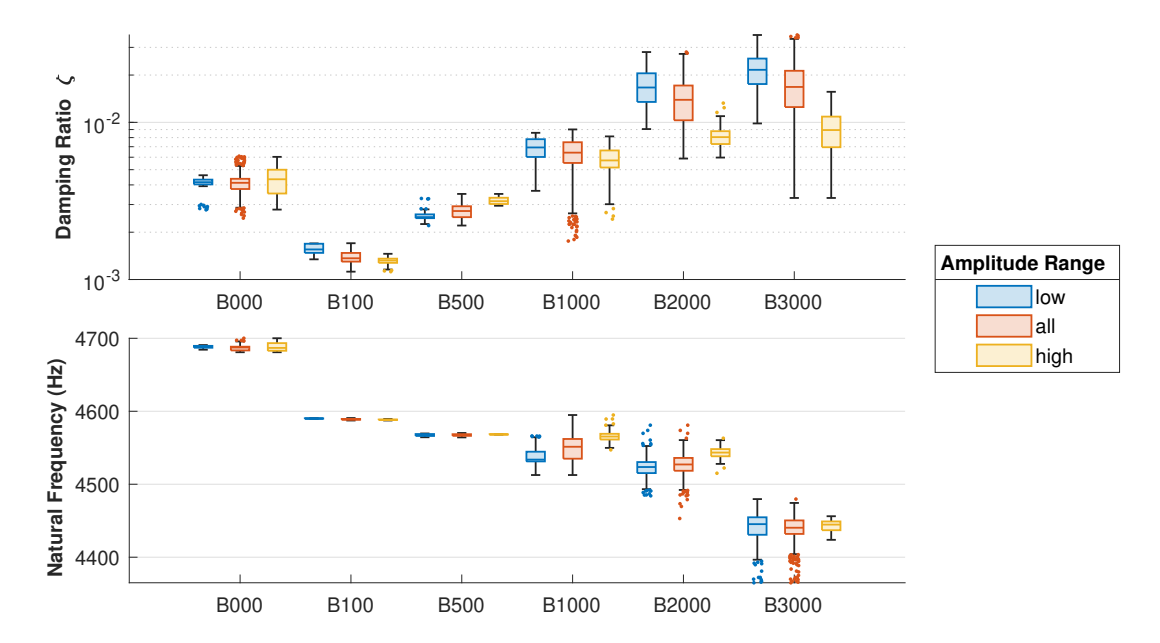


Fig. 18: Summary statistics for damping and natural frequency: Mode T1. The full amplitude range for this mode is $A \in [2.55 \times 10^{-2}, 2.11 \times 10^{1}]g$

The clearest trend that can be observed across all modes as pocket thickness increases is an increase in the median damping. Along with this increase in damping, however, comes an increase in the variability for both damping and natural frequency. This increase in uncertainty is especially pronounced starting with B500 or B1000, depending on the mode.

The solid beam (B000) has very repeatable damping ratio and natural frequency, and it is effectively linear, having nearly the same behavior across all amplitudes. For Mode Z1, for example, the median damping ratio of B000 changes with vibration amplitude from 3.25×10^{-4} to 3.43×10^{-4} , and the natural frequency shifts from $908.29\,\mathrm{Hz}$ to $908.25\,\mathrm{Hz}$ (see Figure 14). These small nonlinearities are likely due to cable damping, aerodynamic drag, and acoustic dissipation, which are expected to be slightly amplitude-dependent. We consider these sources of nonlinearity to be negligible relative to the nonlinearity added by the trapped powder. The damping ratio of Mode Z1 of B3000, for example, changes with amplitude from 5.11×10^{-3} to 5.96×10^{-2} . This shift in damping is over 3000 times larger than the shift for B000, so it seems justified to neglect any nonlinearity due to sources other than the powder.

With respect to vibration amplitude, Mode Z1 has consistently higher damping at high amplitudes, while the opposite trend is seen in most of the other modes, which tend to have lower damping at high amplitudes. Damping that decreases with amplitude is unfortunate because damping is most sorely needed when the vibration amplitude and hence the stresses in a part are highest. In Figures 14 to 18, both trends are seen, depending on the mode, and for a particular mode the trend can change as the pocket thickness increases. Many of the modes exhibit small variability in frequency and damping at the highest amplitudes; it appears that the dominant physics governing the high-amplitude regime are less sensitive to powder state and other sources of variability than those that govern lower amplitude vibrations.

Each mode in Figures 14 to 18 generally shows consistent amplitude-dependent behavior, with some scaling as pocket thickness increases, but each mode behaves in a distinct manner. This variety in nonlinear behavior between modes suggests that various physical mechanisms may be at play. For example, some prior works [9, 23] have suggested that particles trapped in a cavity behave as a secondary mass, which bounces in the pocket at higher vibration amplitudes, in effect becoming separate from the structure. This causes the effective mass of the mode to go down and its frequency to increase, while the collisions with the structure dissipate energy, increasing damping. Another possible explanation for frequency that increases with vibration amplitude is that the powder may stiffen at large strains, due to chains of particles binding, causing the effective stiffness of the powder to increase. Cohesive effects, such as van der Waals forces have also been proposed [17] as a relevant governing mechanism for these parts, due to the small particle diameter of LPBF feedstock.

It is also interesting to note in Figures 14 to 18 that the linear natural frequency of the various modes changes very little as the pocket size increases. The torsion mode (Mode T1) shows the largest change in frequency, decreasing in frequency by 5.3% as the pocket thickness goes from 0 to $3 \, \mathrm{mm}$, and the rest of the modes have nearly constant or

even slightly increasing natural frequency with pocket thickness. The powder pocket location was chosen to be at the center of the beam in part because that region contributes relatively little to stiffness, especially in the bending modes. The decreases in stiffness due to replacing fused metal with loose powder seem to be largely counteracted by the decreased mass. Table B.1 gives the mass of each beam, showing how the overall mass decreases with pocket thickness. Note that these decreases in mass are accompanied by small decreases in the moments of inertia, which could be estimated using the dimensions from Table B.1 and the bulk densities of the fused and unfused metal powder regions².

3.3 Explaining variability: settling and coupling

Such wide error bars as are seen in Section 3.2 could be discouraging to designers hoping to apply this technique for increasing the damping of LPBF parts. One approach could be to use the lower bound of damping, designing conservatively. For example, for B3000 the minimum damping is 0.1-0.3% for most modes, so this value could be used to conservatively predict the life of the structure. Unfortunately, this value is only a little higher than typical material damping. One would like to exploit more of the available damping. If the sources of the variability could be identified, then the uncertainty could be greatly diminished.

If the amplitude of vibration is held constant, then the uncertainty in damping decreases. For example, if it were known that Mode Z1 is to be excited in the high amplitude regime, then the designer could be confident that a 3 mm pocket would contribute at least 3 - 4% damping (see Fig. 14), and up to as much as 7 - 8%. Additionally, the damping in this mode showed little variability at high amplitudes so that damping could be expected to occur reliably.

Our procedure also allows us to investigate the effect of powder state: settled or unsettled. Fig. 19 shows the same data as Fig. 10a, but grouped according to powder state. In the high-amplitude region, we can observe a clear separation between the settled and unsettled behavior, and the variability within each group is much smaller than the total variability seen in Fig. 10a. Therefore, if it is known that the deployed part will be agitated regularly such that the powder will remain in the unsettled state, then the uncertainty in damping for Mode Z1 at high amplitudes is greatly reduced.

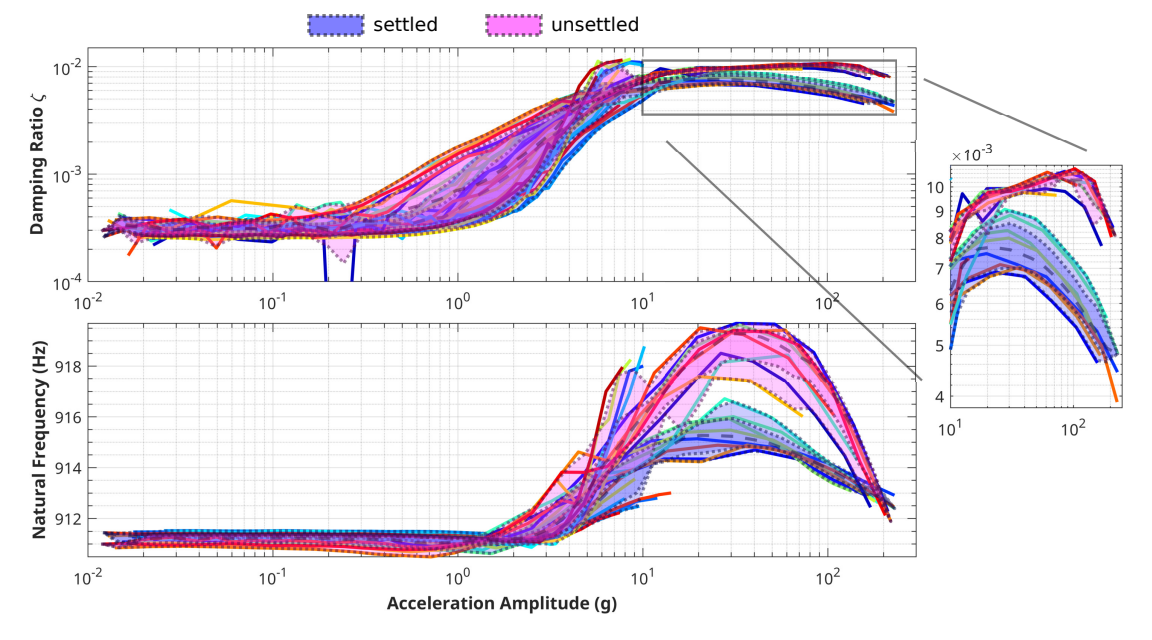


Fig. 19: Damping ratio and natural frequency for Mode Z1 of B1000. The colored envelopes show the bounds (excluding outliers) and interquartile range for the settled and unsettled powder states, as indicated in the legend. Note that while the settled and unsettled powder states behave similarly at vibration amplitudes lower than 10 g, they diverge in the high-amplitude range.

One more consideration that can explain some of the variability in the measurements is the effect of modal interactions, also referred to as modal coupling. Hitting the beam at different locations and with different hammer tips

¹Note that the true moments of inertia will be slightly affected by the extent to which the powder is settled. That effect would likely be negligible, but future work could attempt to quantify it.

²Estimates of these densities are reported in Section B.

excites a different combination of modes. In a system with modal interactions, the nonlinear forces for a given mode can depend on the amplitude of other modes. In that case, we expect that changing the hammer tip and drive point may affect the identified nonlinear damping and natural frequency.

Figure 20 shows the same data as Fig. 19 (Mode Z1 of B1000), but grouped now by powder state, drive point, and hammer type. A clear separation can be seen between the two hammer types, but changing the drive point appears to have no significant effect. Tapping the beam at Z090M should excite only the odd-numbered Z-bending modes, while tapping at Z002B should excite all Z-bending and torsional modes. The dependence of this mode on hit force but not drive point may indicate time-dependent behavior, rather than modal interactions.

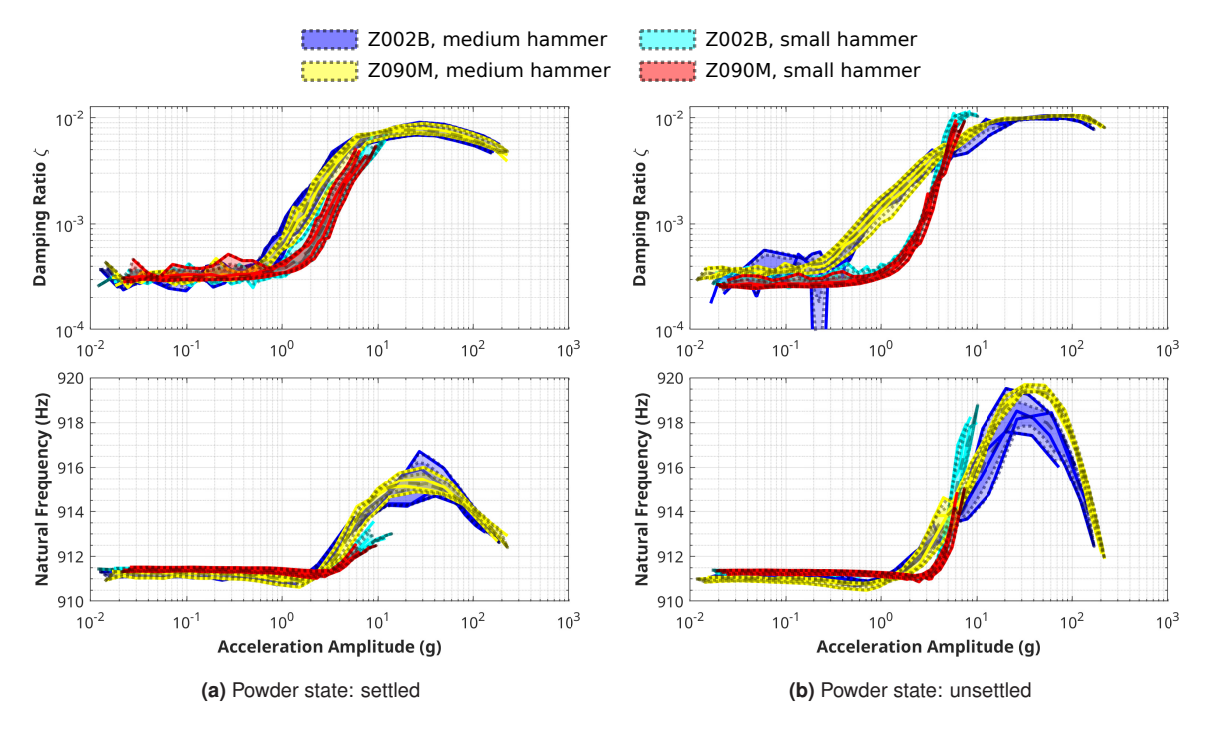


Fig. 20: Damping ratio and natural frequency for Mode Z1 of B1000. The data are grouped according to powder state, drive point, and hammer type. The colors represent drive point and hammer type as indicated in the legend. Drive point Z090M is along a node line for the torsional modes and the even-numbered soft direction (Z) bending modes. The transparent envelopes and dashed lines are interpreted as those in Fig. 10.

The response of the Mode Z2, however, depends strongly on the drive point, as can be seen in Fig. 21. When holding the drive point, hammer type, and powder state constant, the damping and frequency are remarkably repeatable, compared to the large variability seen in Fig. 10b. It seems that modal interactions likely account for most of the variability in this mode. Note that the red curve, which corresponds to striking the beam with the small hammer near the nodal line of Mode Z1, has much lower damping at low amplitudes. This suggests that high damping may only be seen for this mode at low amplitudes when either Mode Z1 or the rigid body modes are also present.

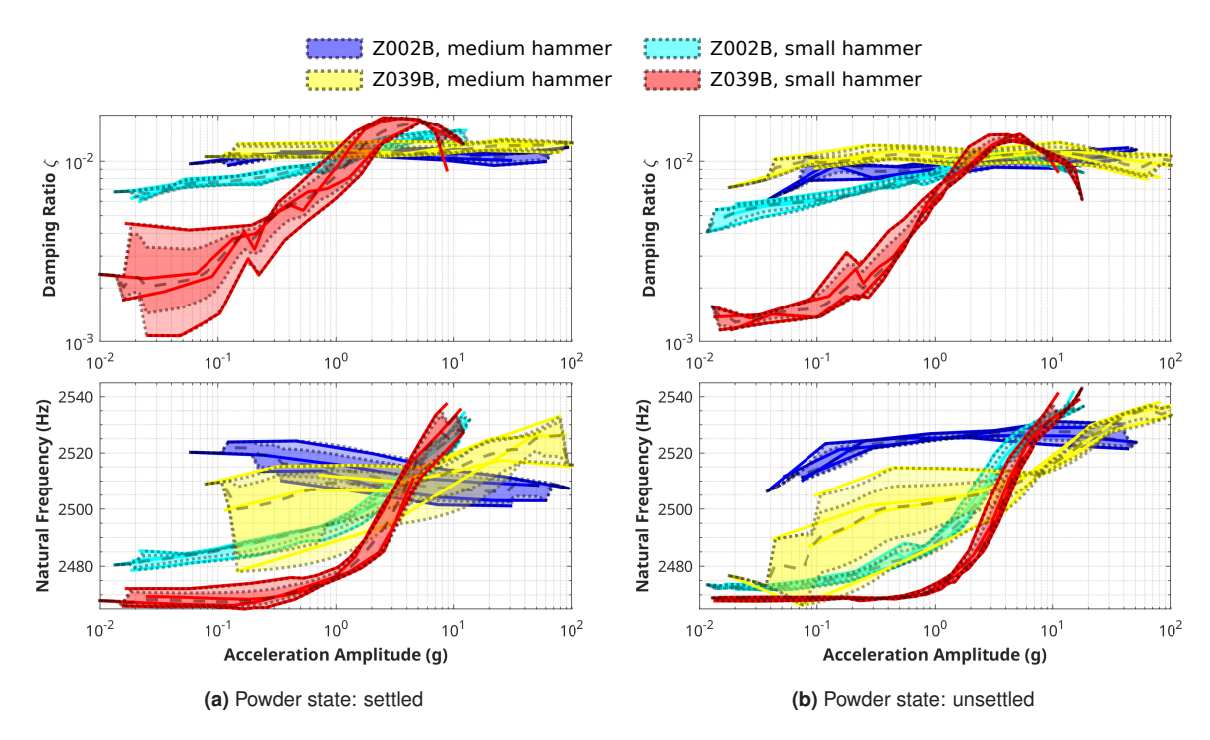


Fig. 21: Damping ratio and natural frequency for Mode Z2 of B1000. The data are grouped according to powder state, drive point, and hammer type. The colors represent drive point and hammer type as indicated in the legend. Drive point Z039B is along a node line for Mode Z1. The transparent envelopes and dashed lines are interpreted as those in Fig. 10.

For each beam and mode, these factors—amplitude-dependence, powder state, drive point, and the hammer used—affect the damping and natural frequency in different amounts. For Mode Z2 of B1000, for example, modal interactions are the most important factor to control for, as shown in Fig. 21. Mode Z1, however, is more sensitive to vibration amplitude and powder state, as can be seen by comparing Figures 19 and 20. A quantitative comparison of the relative importance of each of these factors is presented in Section 3.4.

3.4 Quantifying the importance of each factor

Seeing that powder state, drive point, and the hammer used each had a significant effect for some modes of some beams, but not all, we desired to quantify the relative importance of each variable. It would be beneficial to identify conditions under which some of these factors may be neglected because it may be impractical to control each of these factors in every application. The design process could be accelerated by identifying which of these factors is the most important to consider.

In Section 3.3, a qualitative analysis was performed by inspecting plots where the frequency and damping curves were grouped according to powder state, drive point, and hammer type. It was observed that separating the data into these groups greatly decreased the variability within each group. To quantify these observations, we consider several models for the data, each of which takes different variables into consideration, and investigate the model mismatch error for each. The estimated variance of the model mismatch distribution then serves as a metric to compare these models, which allows us to compare the degree to which each factor was able to explain the variability in the data.

The simplest model which could be proposed for the measurements requires no knowledge of vibration amplitude, powder state, or any other variable. Rather, the damping and natural frequency for the given mode are treated as constant, as in a linear time-invariant system. A simple mean value then becomes the model prediction for all data points, as follows:

$$\hat{y}_i = \frac{1}{N} \sum_{j=1}^{N} y_j \tag{12}$$

where \hat{y}_i is the model prediction for measurement y_i and N is the total number of measurements. The variable y is used here, generically, to refer to either damping ratio or natural frequency, as the analysis is the same for each.

Next, consider a model that accounts for amplitude only. This would be typical of an experiment that quantifies amplitude-dependence but ignores the effects of powder state and modal interactions. Rather than requiring a specific, parametric model form for the nonlinearity, the present analysis will separate the amplitude range into bins and treat each data point within a given bin as coming from the same distribution. This is also the approach that was taken to calculate the statistics represented graphically by the envelopes in Fig. 10 and similar figures in this paper. The model prediction for data point y_i in this model is as follows:

$$\hat{y}_i = \frac{1}{|S|} \sum_{j \in S} y_j \tag{13}$$

where S is the set of indices corresponding to those points belonging to the same amplitude bin as point y_i and |S| refers to the number of elements in S.

A similar approach is used to define more complicated models that account for powder state, drive point, and hammer used. The only modification to Equation (13) is that the set S is restricted to include only those points which the model considers as coming from the same distribution as y_i . For example, a model that accounts for 2 powder states (settled and unsettled) and 50 amplitude bins would subdivide the data into 100 subsets, and the mean in Equation (13) would involve only those points that fall in the same amplitude bin and powder state as the point in question y_i .

For each model, the variance σ^2 of the model mismatch distribution is estimated as follows:

$$\sigma^2 = \frac{1}{N - P} \sum_{i=1}^{N} (y_i - \hat{y}_i)^2 \tag{14}$$

where P is the number of parameters in the model, which is equal to the number of subsets that the data was partitioned into because one mean is calculated for each partition of the data. This results in an unbiased estimate of the variance [24].

First, we compare models that account for only one of the independent variables: amplitude (A), powder state (PS), drive point (DP), or hammer type (HT). The standard deviations σ of the model mismatch for each model are compared in Fig. 22. Note that amplitude (A) is always the most informative variable, typically decreasing uncertainty by a factor of 2 or more. However, in some cases the model including all variables (A, PS, DP, HT) has significantly lower uncertainty.

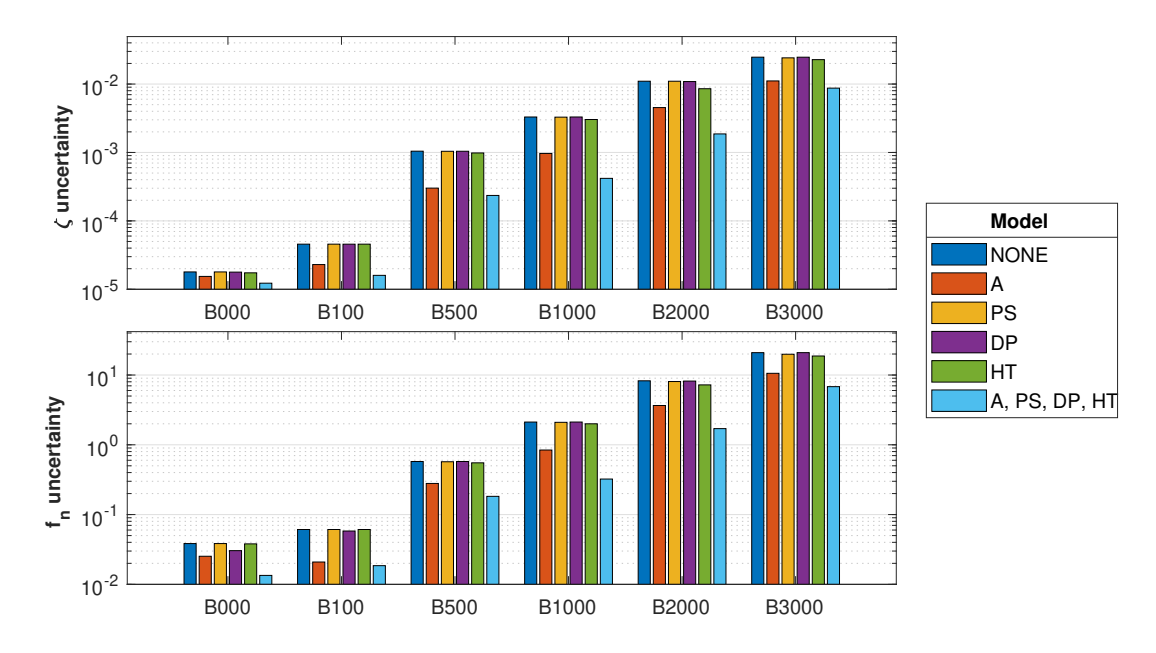


Fig. 22: Standard deviation of model mismatch for several models: Mode Z1. Each model is labeled in the legend according to the variables that it considers. The model labeled "NONE" is the linear model, as in Equation (12). Note that B000 and B100 did not vary the powder state, so the bar "PS" is identical to the bar "NONE". B100 was only tested with one hammer, so "HT" is the same as "NONE".

In order to better determine which of the variables PS, DP, and HT have the largest effect after accounting for amplitude, several two-variable models are compared in Fig. 23. The uncertainties in this plot are normalized against the linear model uncertainty, to facilitate comparison between beams. The model that accounts for amplitude only (A) is included again, for reference, along with the model that includes all variables (A, PS, DP, HT).

These charts can be understood better by comparing the bars for B1000 in Figure 23 to Figures 19 and 20. Mode Z1 displays significant amplitude-dependence, as reflected in the large reduction in the height of bar "A" relative to the linear model (normalized to 1). Next, we observe that accounting for powder state as in Figure 19 reduces the uncertainty further by a significant amount. Without accounting for powder state, the other variables, DP and HT, don't appear to reduce the uncertainty significantly (see the bars "A, DP" and "A, HT"), but the lowest uncertainties are only seen when accounting for all four variables, as in the bar "A, PS, DP, HT" and in Figure 20.

The reduction in uncertainty of the amplitude-dependent model (A) relative to the linear model (normalized to 1) can be interpreted as measuring the nonlinearity of this mode for each beam. For example, the uncertainty in damping for Mode Z1 of B1000 is approximately 30% of that of the linear model, so the uncertainty can be reduced by an average of 70% by accounting for amplitude-dependence of the damping. One caveat to this interpretation is that the uncertainties presented are an average over the data collected in this study. In any given amplitude range, the true reduction in uncertainty may be greater or smaller than this value, and the values presented are biased towards amplitude ranges that have more data points. Additionally, a large reduction in uncertainty for "A" relative to the linear model does not necessarily imply that there is a large nonlinear effect in an absolute sense. For example, the normalized uncertainty in frequency for B100 reduces to 0.34 when accounting for amplitude (bar B100 "A" in Fig. 23), but the entire range of values is only $909.6-909.9\,\mathrm{Hz}$ (see Fig. 14), which would generally be considered a negligible change in frequency. These bar charts serve to compare the relative size of the contributions of various factors to the total uncertainty.

Comparing the effect of powder state, drive point, and hammer type, we see that, with the exception of B000 and B100 for which the powder state was not varied, powder state seems to be the most influential variable for reducing uncertainty in Mode Z1. Another observation from Figure 23 is that the extent to which nonlinearity and the other variables can explain the uncertainty increases with pocket thickness until B1000, after which the unexplainable variability (represented by the uncertainty of the "A, PS, DP, HT" model) increases again. This seems to indicate that nonlinearities due to the powder become increasingly relevant as pocket thickness increases, but that the behavior becomes increasingly complex, uncertain, and difficult to explain as the pocket thickness increases beyond 1 mm.

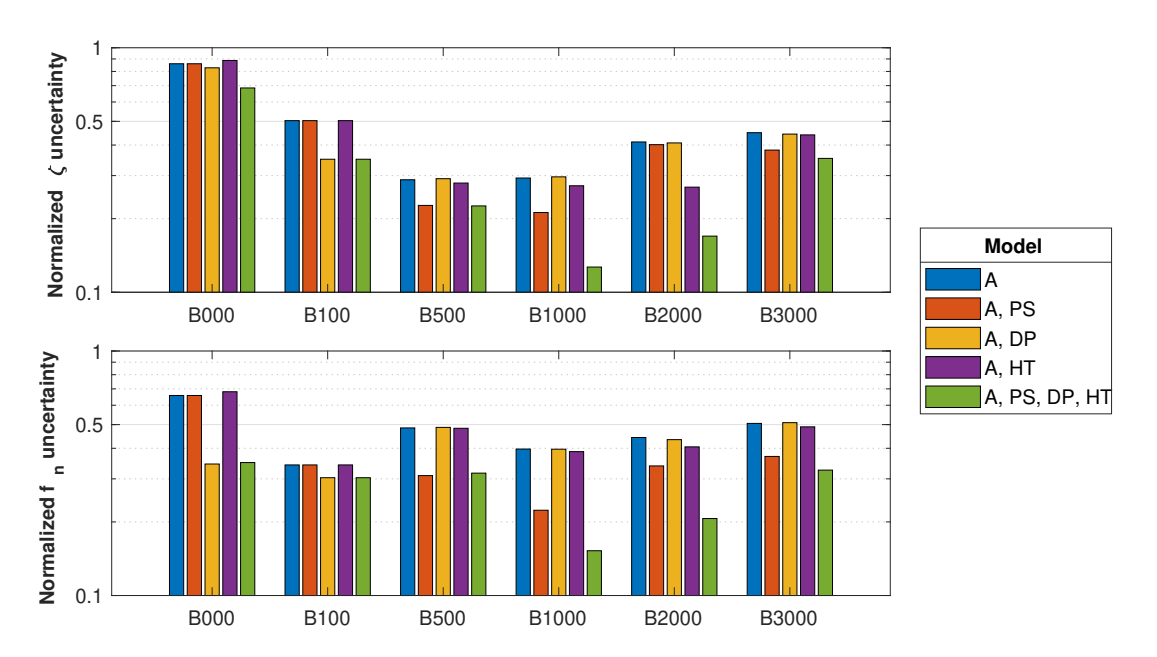


Fig. 23: Normalized standard deviation of model mismatch for several models: Mode Z1. The normalization is done by dividing by the uncertainty of the linear model. Note that B000 and B100 did not vary the powder state, so the bar "A, PS" is identical to the bar "A". B100 was only tested with one hammer, so "A, HT" is the same as "A".

The trends that could be identified for Mode Z1 do not generalize well to the other modes. Figures 24 and 25 compare the normalized uncertainties for the same set of models for Mode Y1 and Mode T1. Each variable—powder

state, drive point, and hammer type—is important for at least one combination of mode and beam pocket thicknesses. Charts like these for every mode studied are available in the supplementary files.

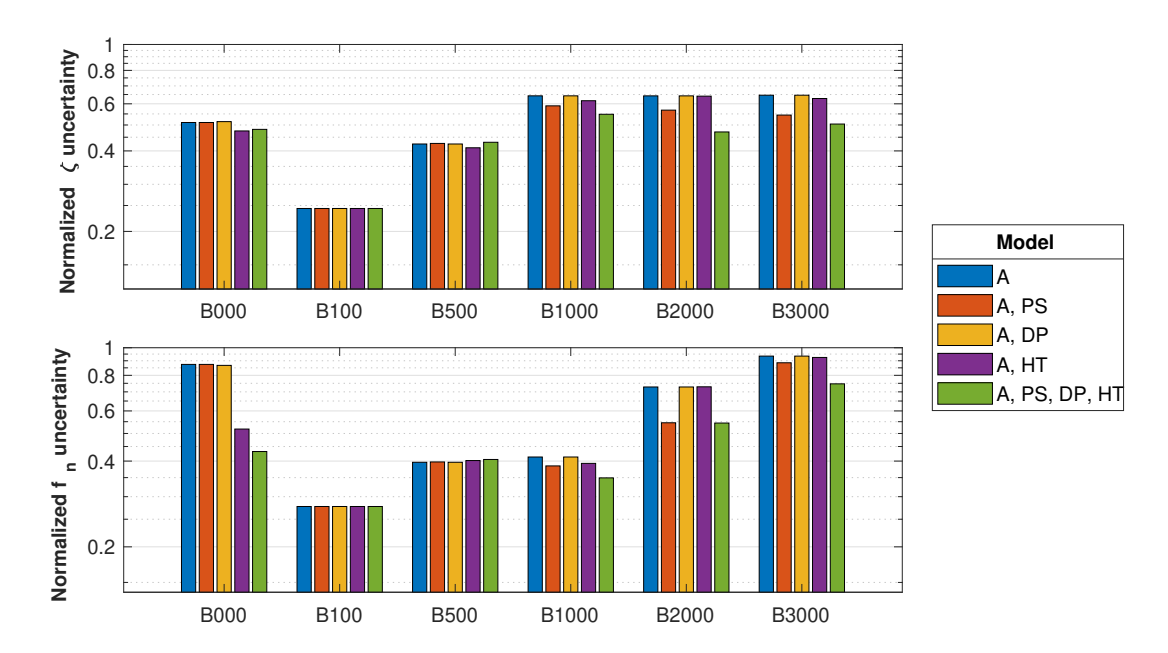


Fig. 24: Normalized standard deviation of model mismatch for several models: Mode Y1. The normalization is done by dividing by the uncertainty of the linear model. Note that B000 and B100 did not vary the powder state, so the bar "A, PS" is identical to the bar "A". B100 was only tested with one hammer, so "A, HT" is the same as "A". Note that because there was only one drive point in the Y-direction, the model "A, DP" is the same as "A" (except for B000, which had two drive points in the Y-direction).

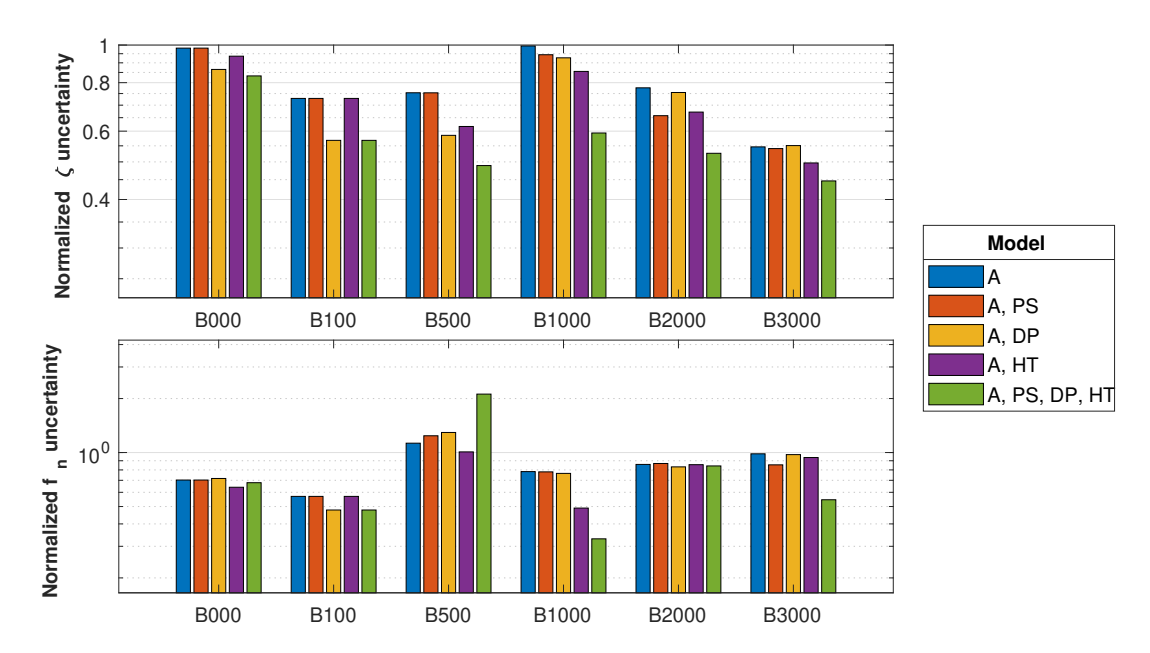


Fig. 25: Normalized standard deviation of model mismatch for several models: Mode T1. The normalization is done by dividing by the uncertainty of the linear model. Note that B000 and B100 did not vary the powder state, so the bar "A," PS" is identical to the bar "A". B100 was only tested with one hammer, so "A, HT" is the same as "A". For B500, this mode was very close in frequency to Mode Z3, so only a few points could be extracted from each hit, which explains the unusually high uncertainties.

4 Conclusions

Six LPBF beams with trapped-powder dampers of varying thicknesses were characterized over a range of vibration amplitudes, powder states, excitation forces, and impact locations. As pocket thickness was increased, the added damping increased, but so did the potential nonlinearity and variability. For the largest powder pockets considered here, the damping typically increased by at least a factor of 10 and often by more than a factor of 100 at some vibration amplitudes, while the natural frequency typically decreased by less than 5%. The highest damping ratios observed were about 10% of critical, although all modes/beams that exhibited damping that high also exhibited nonlinearity and increased uncertainty. For several modes the minimum (or worst case) damping observed, irrespective of amplitude and uncertainty, was as high as 1% of critical, although some modes only saw increases of $2\times$ or so compared to material damping, which was about 0.05% of critical. In any event, the results show that this could be an effective means of adding damping to various modes of LPBF parts, although one must consider nonlinearity and variability to realize the maximum benefit.

In addition to amplitude-dependence, the modal damping and natural frequencies of these samples exhibited significant variation with the assumed powder state, hit force, and impact location. The dependence on impact location is thought to indicate nonlinear modal coupling. The manner in which the damping and frequency depend on each of these factors was found to vary greatly between modes and pocket thicknesses. The relative importance of these factors was quantified, and it was found that each factor dominates for at least one of the modes studied. Hence, while many of these effects could likely be neglected in practical applications, in some cases they would contribute to significantly higher uncertainty in the observed modal damping if not accounted for.

While we were unable to directly observe the powder state in these experiments, several factors point to its influence on the results. Strictly speaking, the LPBF parts with trapped-powder dampers were found to exhibit an unknown memory effect, in which different kinds of agitation caused the system to transition between a high-damping state and a low-damping state. We found these state transitions to be reversible, and we hypothesized this behavior to be caused by powder settling and unsettling.

One implication of these findings is that care must be taken when testing parts with trapped-powder dampers to account for the packing state somehow. For example, studies that compare damping between multiple specimens with trapped-powder dampers should handle the samples in a consistent manner and either identify or control the packing state. Perhaps all the samples could be tapped a set number of times before testing to encourage consistent powder settling. We found that even turning the parts upside down briefly was sufficient agitation to cause significant changes in their damping behavior, so care should be taken to handle parts consistently. Failure to do this could lead to erroneous conclusions being drawn from comparisons between one part with settled powder and another with unsettled powder. Another approach would be to find upper and lower bounds on the damping behavior of each sample by intentionally driving the system between the most packed and unpacked states. This was the approach taken in the present study.

These findings also have important implications if one wishes to employ this method of damping in practice. In the worst case, one could extract the minimum damping from the results in Figures 14 to 18 and use that when performing stress analysis. For example, a minimum damping ratio of 0.001 could be expected for Mode 1 of a beam with a 3 mm powder pocket. This figure is not very impressive, although still significantly better than one would expect for solid 316L stainless steel³. In contrast, if one takes the nonlinearity into account then at higher amplitudes the minimum damping increases to nearly 0.040, which is a rather large value for a metal part. Presumably, large amplitude vibrations are also most likely to damage the part, and so this configuration would have damping when it is needed most, whether the powder is settled or not. Furthermore, if the part is to be deployed in an environment that can be expected to unsettle the powder regularly, then the minimum damping increases further to 0.045 (see supplementary data for B3000, Mode Z1).

Finally, the study presented in Section D confirmed that trapped-powder damping is effective across a wide range of temperatures. At high temperatures (95 $^{\circ}$ C), the damping ratio was observed to decrease slightly, from 0.022 to 0.019 being the largest decrease seen (a 14% decrease), but this effect is likely small enough to be negligible. The performance of viscoelastic damping treatments would be expected to suffer much more (as much as 80% for a typical viscoelastic polymer) over similar changes in temperature.

The raw and processed data and graphs, a subset of which are presented in this paper, are available in the supplementary material. Future work could attempt to identify additional trends and general principles to inform design decisions involving LPBF trapped-powder dampers. This dataset can also be used in the future for model

³One should bear in mind that the support structure does contribute some additional damping and the uncertainty due to the support damping was not quantified here. However, the same bungee types and locations were used in all tests so the support damping is thought to be constant for each mode.

updating and validation.

Appendix

A Supplementary material

The experimental datasets described in this work are publicly available in a Zenodo repository [25], together with the results of the data processing and the complete set of graphs mentioned in Section 3.

B Measurements of beam samples

The dimensions and mass of each beam tested in the present work are given in Table B.1. The mass of each was measured with an A&D EJ-303 balance. The length, L, was measured with a ruler, and the width and height were measured with calipers. Two small adjustments were made to the measured dimensions in an attempt to correct for biases in the measurements. First, most of the beams were slightly curved, and that curvature was estimated to bias the length measurements by $-2\,\mu\mathrm{m}$. Second, because no post-processing was performed to change the as-printed finish, the beams had significant surface roughness that biased the measurements. Based on a study by Zhang and Yuan [26], the as-printed surface roughness profile was estimated to vary around the nominal position of each surface by $r \in [-50, 100]\mu\mathrm{m}$, with the average value being $r = 25\,\mu\mathrm{m}$. The measurements were taken from the peak of the roughness profile on both sides of the part, so $100\,\mu\mathrm{m} - 25\,\mu\mathrm{m} = 75\,\mu\mathrm{m}$ must be subtracted twice in order to estimate the average value of the dimension. Therefore, the total bias due to surface roughness is taken to be $2\times75\,\mu\mathrm{m} = 150\,\mu\mathrm{m}$.

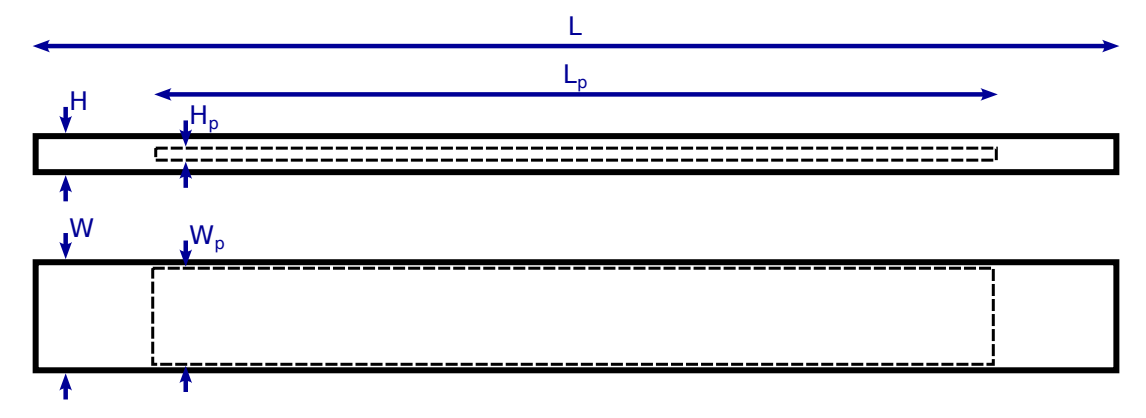


Fig. B.1: Drawing of beam showing the labels used in Table B.1 for the six dimensions.

In order to estimate the (unmeasured) dimensions of the pocket, the following corrections were applied to the nominal pocket dimensions. First, the beams were found to have contracted slightly relative to their nominal dimensions, and this was assumed to have been due to uniform thermal contraction, which would affect the internal pocket dimensions as well as the external dimensions. The ratio between the measured length (after adjusting for curvature and surface roughness⁴) and the nominal length was used as a constant factor of thermal contraction to adjust the nominal pocket dimensions. Finally, $50 \,\mu\text{m}^5$ was subtracted from the contracted pocket dimensions as an estimate of the effect of internal surface roughness on the mean cavity dimensions. These adjustments explain why the values of H_p given in Table B.1 are slightly smaller than the nominal pocket thickness in microns, which is the number following the letter "B" in the beam label. As an example, the length of B1000 was measured to be $179.02 \, \text{mm}$, so the corrected average length was $179.052 \, \text{mm}$ and the contracted nominal length was estimated to be $179.002 \, \text{mm}$.

⁴In this case, the quantity of interest is not the average value of the dimension, but the contracted nominal dimension. Therefore, the difference between the peak of the roughness profile and the nominal position (100 μm) is subtracted twice to estimate the post-contraction nominal dimension.

 $^{^5}$ The difference between the (post-thermal-contraction) nominal position of a surface and the average position of the roughness profile was estimated to be $r=25\,\mu\mathrm{m}$, so this value was subtracted twice in order to correct for the effect of surface roughness on the average pocket dimensions.

The factor of thermal contraction was then 179.002/180 = 0.994, so the internal pocket thickness was estimated to be $1000 \, \mu m \times (0.994) - 50 \, \mu m = 944 \, \mu m$.

		Dimensions (mm)					
Beam label	Mass (g)	L	W	H	L_p	W_p	H_p
B000	151.9	178.70	18.28	5.92	0.00	0.00	0.00
B100	151.5	179.15	18.15	6.00	139.25	15.87	0.05
B500	149.3	179.10	18.10	5.94	139.21	15.87	0.45
B1000	145.5	179.05	18.24	5.85	139.17	15.86	0.94
B2000	138.6	178.85	18.32	5.92	139.02	15.84	1.94
B3000	132.2	178.85	18.15	5.92	139.02	15.84	2.93

These dimensions, along with the measured masses, were then used to estimate the densities of the fused and unfused powder. The composite density of each sample was related to the volume fraction of unfused powder, f_p , by a linear regression, allowing the densities of the fused and unfused powder to be estimated by evaluating that best-fit line at $f_p = 0$ and $f_p = 1$, respectively, as depicted in Figure B.2. There are more than six points in this plot because measurements from other beams besides those included in the present study were used in the density estimate. The densities of the fused and unfused powder regions were found to be $\rho_{fused} = 7.898 \pm 0.019 \, \mathrm{g/cm^3}$ and $\rho_{powder} = 4.892 \pm 0.186 \, \mathrm{g/cm^3}$, where the uncertainties presented represent a single standard error. This results in a filled volume ratio estimate of $\rho_{powder}/\rho_{fused} = 61.9\%$, which falls well within the 0.59 to 0.63 range of packing densities predicted by Xiang et al. [27] by simulation of the LPBF process.

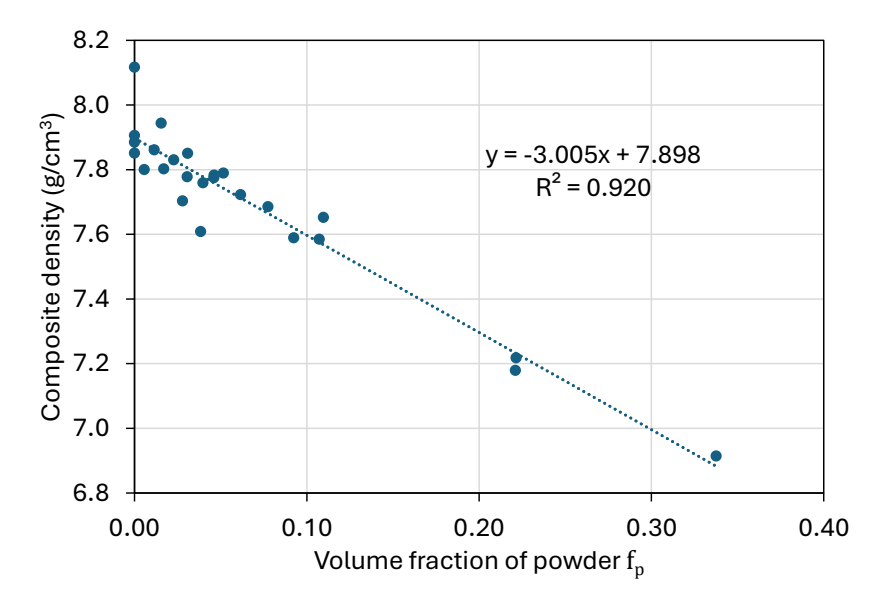
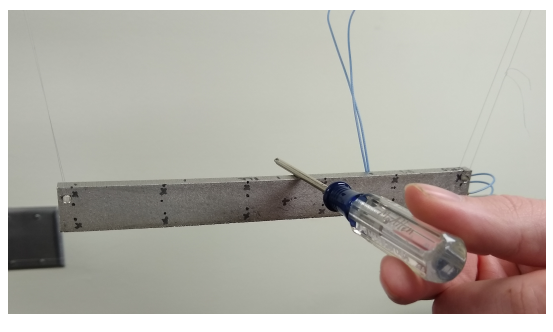
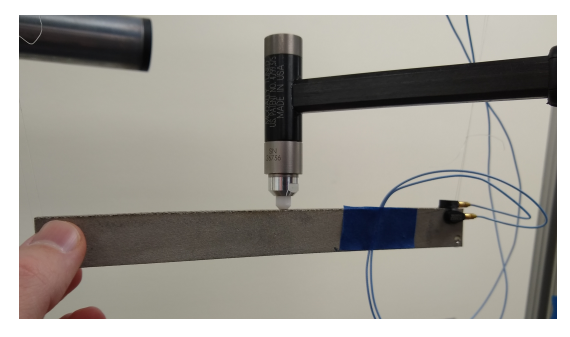


Fig. B.2: Composite density of the beam samples, plotted against the volume fraction of unfused powder in the beam. The best-fit linear regression was used to estimate the density of the fused and unfused powder regions.

C Details of procedure for bounding system behavior

The settling and unsettling procedures used in Phase 2 are based on what worked well in [19] and are described in Table C.1. The settling runs involved striking the beam from above with a small screwdriver (a Craftsman 41293 – V – WF), as shown in Figure C.1a. The unsettling was done by holding the beam upside-down and striking it from above with the medium hammer (a PCB 086C01 with a plastic tip), as shown in Figure C.1b.





(a) Settling hits

(b) Unsettling hits

Fig. C.1: Photos of the two kinds of agitation being performed.

However, as the kind and amount of agitation required to settle or unsettle beams of different pocket thicknesses was expected to differ, some of the details of the procedure varied slightly from beam to beam. The procedure presented in Table C.1 was the most commonly used one, and each Phase 2 procedure was largely the same.

Table C.1: Procedure for Phase 2. The key for decoding the hit location abbreviations is given in Fig. 2. For the runs using the screwdriver, no force measurement was available, so the peak acceleration measured by the hit direction accelerometer was used as a reference to keep hit forces as repeatable as possible.

Run name	Number of hits	Hit location	Implement used	Target force (N) or acceleration (g)	
	10	Y090	screwdriver	250 g	
0.011	5	Y090	screwdriver	150 g	
set1	5	Y090	screwdriver	100 g	
	5	Y090	screwdriver	50 g	
meas1	3	Z002B	medium hammer	150 N	
illeasi	3	Y077	medium hammer	150 N	
	20	Y090	screwdriver	250 g	
set2	10	Y090	screwdriver	150 g	
SEIZ	10	Y090	screwdriver	100 g	
	10	Y090	screwdriver	50 g	
meas2	3	Z002B	medium hammer	150 N	
1116452	3	Y077	medium hammer	150 N	
uns3	10	IY090	medium hammer	150 N	
meas3	3	Z002B	medium hammer	150 N	
meass	3	Y077	medium hammer	150 N	
uns4	20	IY090	medium hammer	150 N	
meas4	3	Z002B	medium hammer	150 N	
1116454	3	Y077	medium hammer	150 N	
	10	Y090	screwdriver	250 g	
set5	5	Y090	screwdriver	150 g	
5613	5	Y090	screwdriver	100 g	
	5	Y090	screwdriver	50 g	
meas5	3	Z002B	medium hammer	150 N	
IIIEass	3	Y077	medium hammer	150 N	
	20	Y090	screwdriver	250 g	
set6	10	Y090	screwdriver	150 g	
2610	10	Y090	screwdriver	100 g	
	10	Y090	screwdriver	50 g	
maaaG	3	Z002B	medium hammer	150 N	
meas6	3	Y077	medium hammer	150 N	

Phase 3 was performed any time that Phase 2 found the powder state to have a significant effect because the settling and unsettling procedures that worked well for one beam did not always work well for another. In general, more hits were required to fully settle the powder for beams with thinner powder pockets, and the unsettling procedure typically required little modification if any.

The procedure for Phase 3 is summarized in Figure C.2. Whichever mode displayed the memory effect most clearly in Phase 2 was chosen for study in Phase 3. Choosing a single mode for consideration in this phase reduces the effort of testing and data analysis: only one drive point is required, and only one mode needs to be analyzed. As this phase may involve several iterations, this reduction in testing and analysis time is significant.

The number of hits, location of hits, and force levels are varied iteratively until a reliable procedure has been identified for settling the powder for the beam in question (see the row titled "Optimizing Settling" in Figure C.2). Then, the procedure is inverted to identify the optimal procedure for unsettling the powder (see the row titled "Optimizing Unsettling" in Figure C.2).

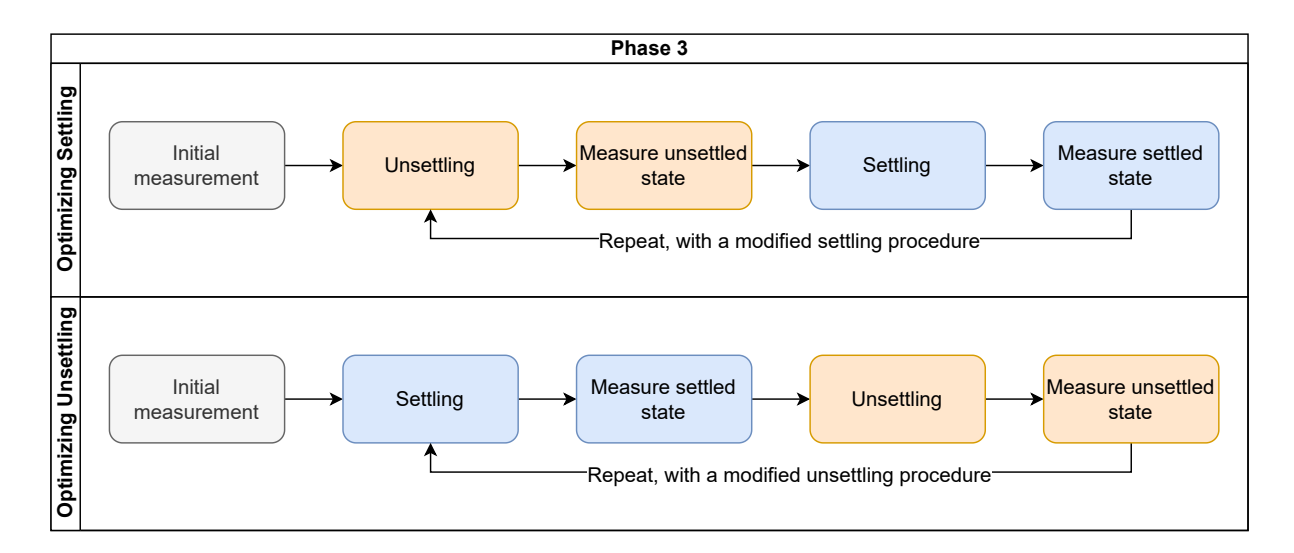


Fig. C.2: Summary of procedure for Phase 3. The boxes labled "Unsettling" and "Settling" stand for the execution of a powder agitation procedure, similar to the runs labeled "uns" and "set" in Table C.1, but with varying numbers, locations, and forces of hits. The boxes beginning with "Measure" stand for a ringdown measurement, performed by tapping the beam with a modal hammer at a location that will excite the mode of interest (the mode identified in Phase 2).

The settling and unsettling procedures should be optimized to maximize the difference between the settled and unsettled states. Typically, this meant designing an unsettling procedure that led to a high-damping state and a settling procedure that led to a low-damping state, but occasionally the changes in natural frequency were also significant. It is also desirable to identify the minimum number of hits required to cause convergence to a fully settled or unsettled state, as this will greatly shorten the execution of Phase 4.

D Varying the operating temperature

As discussed in Section 1, viscoelastic damping treatments are known to be highly temperature-dependent, providing optimal damping performance only in a narrow temperature range [4]. Trapped-powder dampers are not expected to have their performance impacted by operating temperature, as long as it remains below the sintering temperature of the powder [14], which would be one of the main advantages of this technique over viscoelastic damping treatments. While it seems to be generally believed that powder dampers will be less sensitive to temperature than viscoelastic dampers, the authors were unable to find any studies where the damping contribution of LPBF trapped-powder dampers was measured at various operating temperatures. Additionally, it is known that the material properties of steel, including the friction coefficient, can vary somewhat with temperature [28], so it is reasonable to expect some slight dependence of the damping ratio on temperature. Therefore, the present study measured one beam (B2000) at three different temperatures to determine whether there was any significant dependence on temperature.

D.1 Methods: Varying temperature

The setup for these tests was the same as described in Section 2.1, excepting a few modifications. Only one accelerometer was attached to the beam, the one that measured in the Z-direction, and it was mounted with the wire facing outwards instead of being taped at the node line of Mode 1. This was done to avoid heating the accelerometer wires directly, as well as due to concerns about the performance of the tape at high temperatures. Additionally, the accelerometer was attached with DuraKore dental cement from Reliance Dental Manufacturing instead of Super Glue, and the fishing line was replaced with 0.2 mm diameter aramid thread. Beam temperatures were measured with a FLIR E50 infrared (IR) camera.

The general outline for these tests consists of the following steps:

- 1. tap the beam repeatedly until it reaches a consistent, stable powder state;
- 2. measure the beam's behavior;
- 3. heat or cool the beam;
- 4. measure the beam at the new temperature;
- 5. wait for the beam to return to room temperature;
- 6. measure the beam again.

While the procedure described in Section 2.4 drives the beam to the most settled and unsettled states in order to find upper and lower bounds, this procedure accounts for the possibility of change in the powder state by quantifying any drift in behavior over the course of the experiment. Step 1 is performed because some powder states have been found to be more stable than others: after repeated measurement taps, the beam tends towards a relatively repeatable state. Reaching this state before continuing with the rest of the procedure should help to keep the powder state relatively consistent throughout the experiment. Between steps 2 and 6, care is taken to avoid jostling the beam, with exception of the measurement impacts, again so as to minimize the likelihood of large shifts in powder state. Ultimately, the effect of any drift in powder state can be estimated by comparing the measurements taken in step 2 to those taken in step 6. Identifying the effect of changes in powder state gives us confidence that any trends we attribute to operating temperature are not merely due to changing powder state.

For the low-temperature tests, step 3 consisted of carefully transporting the beam, with the accelerometer wire still attached, into a standard household freezer to cool overnight. Leaving the accelerometer wire attached allowed for quicker reconnection to the data acquisition system after the beam was removed from the freezer. (The temperature in the freezer was $-18\,^{\circ}$ C.) Next, we quickly transported the beam back to our testing setup and immediately performed the step 4 measurements. For the high-temperature tests, step 3 was performed by holding a heat gun (Master HG-501A) underneath the beam and moving it side to side while pointed upwards. The IR camera was used to ensure that the beam was heated evenly. Figure D.1 shows an example frame from the video recorded by the IR camera during high-temperature testing, taken a few seconds before the measurement taps were performed. Note that temperature of the beam appears to be relatively uniform, between $90\,^{\circ}$ C and $100\,^{\circ}$ C.

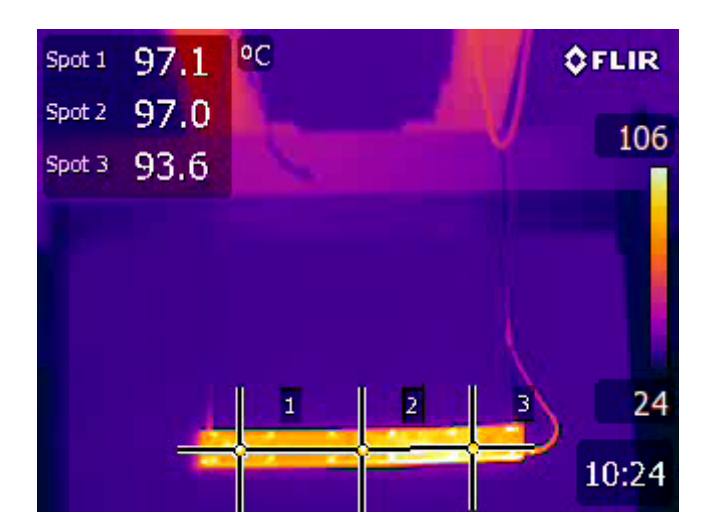


Fig. D.1: Picture from the IR camera taken a few seconds before tapping the beam to measure its behavior at elevated temperatures. Compare to Figure 1a. The bright spots appearing in a grid should be ignored, as they correspond to locations that were marked with black ink (see Figure 1b), suggesting that the ink affects the emissivity of the surface.

The measurement runs in steps 2, 4, and 6 consisted of five measurement taps at Z090M with the small hammer, aiming for forces of 50 N. The ring-down measurements were processed as described in Section 2.2. The first soft-direction bending mode (Mode Z1) was the only mode considered in this study. We expect that the effect of operating temperature on the damping performance of this mode will be representative of its effect on other modes.

D.2 Results: Varying temperature

Figure D.2 shows the results from the experiment described in Section D.1, in which the operating temperature was varied. The clearest trend in the data is that the natural frequency shifts with temperature: cooling the beam shifted the natural frequency upward by approximately $6\,\mathrm{Hz}$, and heating the beam shifted the frequency downward by about $26\,\mathrm{Hz}$. This effect is likely due to the steel having temperature-dependent stiffness. To quantify the change in stiffness that this assumption implies, we consider the following relationships:

$$\omega_n \propto \sqrt{E}$$
 (D.1)

$$\frac{E_2}{E_1} = \left(\frac{\omega_{n2}}{\omega_{n1}}\right)^2 \tag{D.2}$$

where ω_n is the frequency of a given mode of a part, E is the Young's modulus of that part, the symbol ∞ represents proportionality, and the numbered subscripts represent two conditions that differ only by the Young's modulus. Applying Equation (D.2) to natural frequencies read from the low-amplitude range of Figure D.2 gives the following: cooling the beam by 14 °C resulted in a 1.4% increase in stiffness, and heating the beam by 73 °C resulted in a 5.7% decrease in stiffness. For comparison, we consider the measurements by Rehmer et. al [29] of the temperature-dependent elastic modulus of 316L stainless steel. Interpolating (and extrapolating, slightly) on their data, we would expect a 0.60% increase in stiffness for the cold tests and a 3.1% decrease in stiffness for the high-temperature tests. Our results suggest nearly double those amounts, which could perhaps be explained by uncertainties in the temperatures measured by the IR camera and in the damping values from Figure D.2. It is also possible that some other effect related to uneven heating or thermal expansion contributes to this shift in natural frequency.

Perhaps of greater interest is the effect of temperature on the damping ratio. Looking at the results from the cold test in Figure D.2a, no significant effect on damping can be seen, except perhaps a very slight increase in damping at high amplitudes. The hot test results in Figure D.2b present a slight decrease in damping ratio with temperature. While this effect is small, it appears to be significant in the statistical sense. A slight reduction in damping with increase in temperature is consistent with the results of [28], in which the friction coefficient of steel on steel contact was found to decrease at high temperatures. Within the temperature ranges studied here, however, the effect of operating temperature on damping ratio can be neglected. This slight reduction in damping with very high temperatures is still

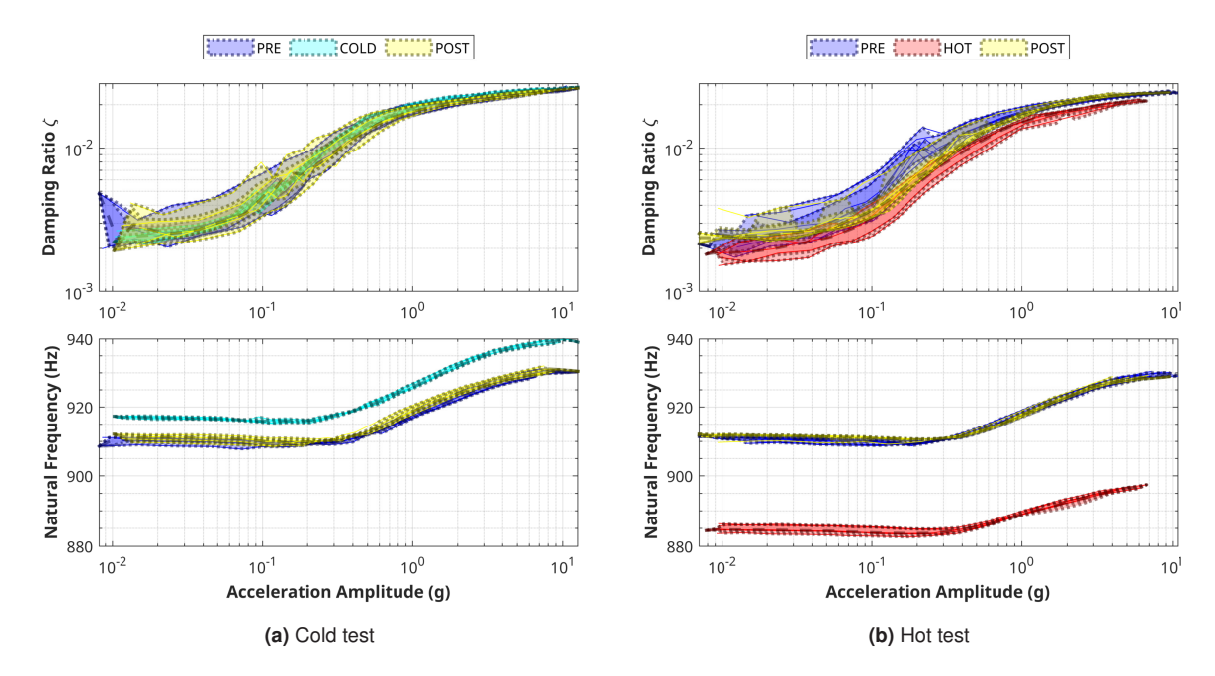


Fig. D.2: Damping ratio and natural frequency for Mode Z1 of B2000, testing at several temperatures. The data labeled "COLD" were taken at approximately 8 °C and the data labeled "HOT" were taken at approximately 95 °C. The data labeled "PRE" and "POST" were taken at room temperature (22.2 °C) before and after the tests at different temperatures. The transparent envelopes and dashed lines are interpreted as those in Fig. 10.

greatly preferable to the large decreases in damping that one would expect for a viscoelastic material operating in a similar range of temperatures. For example, the loss factor of a typical viscoelastic damping polymer [30] can drop by as much as 80% over a 70 °C temperature change.

Authors' Contributions

J. Black designed and led the experiments, performed visualization and analysis of the results, and wrote the majority of the paper. B. Andrus and D. Koski performed most of the experiments and data processing, as well as helping to draft the sections on varying temperature. M. Allen provided technical expertise and guidance on modal testing and nonlinear system identification, advisory support throughout the entire process, and edited the manuscript. N. Crane and T. Nelson contributed to the ideation and planning of the project, lending their expertise in additive manufacturing and materials science. All authors reviewed the final manuscript.

Acknowledgements

Much of the work reported in this paper was supported by the National Science Foundation (NSF) under Grant Number CMMI-2348509. The authors gratefully acknowledge the work of Samuel Teng, who created the beams used here as part of his master's thesis [20].

References

- [1] O. Diegel, A. Nordin, and D. Motte. A practical guide to design for additive manufacturing. Springer, 2019. ISBN 981-13-8281-6.
- [2] C. Beards. Damping in Structural Joints. The Shock and Vibration Digest, 11(9):35-41, 1979.
- [3] Lazan, B. J. Fatigue Failure Under Resonant Vibration Conditions. Technical Report WADC TR 54-20, Wright Air Development Center, Wright-Patterson Air Force Base, OH, 1956.
- [4] R. Lakes. Viscoelastic Materials. Cambridge University Press, Cambridge, 2009. ISBN 978-0-521-88568-3. doi:10.1017/CBO9780511626722.

- [5] H. V. Panossian. Structural Damping Enhancement Via Non-Obstructive Particle Damping Technique. *Journal of Vibration and Acoustics*, 114(1):101–105, 1992, URL http://dx.doi.org/10.1115/1.2930221. Number: 1.
- [6] J. J. Hollkamp and R. W. Gordon. Experiments with particle damping. volume 3327 of *Proceedings of SPIE The International Society for Optical Engineering*, pages 2–12. SPIE, 1998. ISBN 0277786X. doi:10.1117/12.310675.
- [7] S. E. Olson. An analytical particle damping model. *Journal of Sound and Vibration*, 264(5):1155–1166, 2003. ISSN 0022-460X. doi:https://doi.org/10.1016/S0022-460X(02)01388-3.
- [8] Z. Xu, M. Y. Wang, and T. Chen. A particle damper for vibration and noise reduction. *Journal of Sound and Vibration*, 270(4–5): 1033–1040, 2004. ISSN 0022-460X. doi:10.1016/S0022-460X(03)00503-0. Number: 4–5.
- [9] Z. Lu, Z. Wang, S. F. Masri, and X. Lu. Particle impact dampers: Past, present, and future. Structural Control and Health Monitoring, 25(1):e2058, 2018. ISSN 1545-2263. doi:10.1002/stc.2058. _eprint: https://onlinelibrary.wiley.com/doi/pdf/10.1002/stc.2058.
- [10] T. Künneke and D. Zimmer. Funktionsintegration additiv gefertigter Dämpfungsstrukturen bei Biegeschwingungen. In H. A. Richard, B. Schramm, and T. Zipsner, editors, *Additive Fertigung von Bauteilen und Strukturen*, pages 61–74. Springer Fachmedien Wiesbaden, Wiesbaden, 2017. ISBN 978-3-658-17780-5. doi:10.1007/978-3-658-17780-5
- [11] O. Scott-Emuakpor, T. George, B. Runyon, C. Holycross, B. Langley, et al. Investigating Damping Performance of Laser Powder Bed Fused Components With Unique Internal Structures. In *Volume 7C: Structures and Dynamics*, page V07CT35A020, Oslo, Norway, June 2018. American Society of Mechanical Engineers. ISBN 978-0-7918-5115-9. doi:10.1115/GT2018-75977.
- [12] T. Schmitz, M. Gomez, B. Ray, E. Heikkenen, K. Sisco, et al. Damping and mode shape modification for additively manufactured walls with captured powder. *Precision Engineering*, 66:110–124, November 2020. ISSN 0141-6359. doi:10.1016/j.precisioneng.2020.07.002.
- [13] H. Guo, R. Yoneoka, and A. Takezawa. Influence of cavity partition on the damping performance of additively manufactured particle dampers. *Powder Technology*, 439:119675, April 2024. ISSN 00325910. doi:10.1016/j.powtec.2024.119675.
- [14] T. Ehlers, M. Oel, S. Tatzko, G. Kleyman, J. Niedermeyer, et al. Design Guidelines for Additive Manufactured Particle Dampers: A Review. *Procedia CIRP*, 119:891–896, January 2023. ISSN 2212-8271. doi:10.1016/j.procir.2023.03.134.
- [15] J. Westbeld, F. Von Coburg, and P. Höfer. Forced-response characterization of PBF-LB/AlSi10Mg particle dampers with thin and flat cavities. *Progress in Additive Manufacturing*, 8(4):745–757, August 2023. ISSN 2363-9512, 2363-9520. doi:10.1007/s40964-023-00428-5.
- [16] H. Shu, S. A. Smith, and M. R. W. Brake. The Influence of Additively Manufactured Nonlinearities on the Dynamic Response of Assembled Structures. *Journal of Vibration and Acoustics*, 142(1):011019, February 2020. ISSN 1048-9002, 1528-8927. doi:10.1115/1.4045381.
- [17] D. Kiracofe, D. Diaz, M. Postell, D. Celli, J. Hollkamp, et al. Understanding the Role of Attractive Forces in Additively Manufactured Parts With Internal Particle Dampers. In Volume 11B: Structures and Dynamics — Emerging Methods in Engineering Design, Analysis, and Additive Manufacturing; Fatigue, Fracture, and Life Prediction; Probabilistic Methods; Rotordynamics; Structural Mechanics and Vibration, page V11BT23A002, Boston, Massachusetts, USA, June 2023. American Society of Mechanical Engineers. ISBN 978-0-7918-8706-6. doi:10.1115/GT2023-102685.
- [18] O. Scott-Emuakpor, L. Sheridan, B. Runyon, and T. George. Vibration Fatigue Assessment of Additive Manufactured Nickel Alloy With Inherent Damping. *Journal of Engineering for Gas Turbines and Power*, 143(10):101009, September 2021. ISSN 0742-4795. doi:10.1115/1.4051489. _eprint: https://asmedigitalcollection.asme.org/gasturbinespower/article-pdf/143/10/101009/6753625/gtp_143_10_101009.pdf.
- [19] J. K. Black, S. Clawson, M. S. Allen, N. Crane, and T. Nelson. Nonlinear dynamic properties of powders in additively manufactured steel beams. In *Proceedings of ISMA*, Leuven, Belgium, September 2024.
- [20] S. H. Teng. Investigating the Effects of Unfused Powder Damping in Laser Powder Bed Fusion. PhD thesis, Brigham Young University, Provo, UT, 2023, URL https://scholarsarchive.byu.edu/etd/10219/.
- [21] M. Feldman. Non-linear system vibration analysis using Hilbert transform—I. Free vibration analysis method 'Freevib'. *Mechanical Systems and Signal Processing*, 8(2):119–127, 1994. doi:https://doi.org/10.1006/mssp.1994.1011. Number: 2.
- [22] B. Deaner, M. S. Allen, M. J. Starr, D. J. Segalman, and H. Sumali. Application of Viscous and Iwan Modal Damping Models to Experimental Measurements From Bolted Structures. ASME Journal of Vibrations and Acoustics, 137:12, 2015. doi:10.1115/1.4029074.
- [23] Y. Harduf, E. Setter, M. Feldman, and I. Bucher. Modeling additively-manufactured particle dampers as a 2DOF frictional system. Mechanical Systems and Signal Processing, 187:109928, March 2023. ISSN 0888-3270. doi:10.1016/j.ymssp.2022.109928.

- [24] W. Navidi. Statistics for engineers and scientists. McGraw-Hill Education, New York, NY, fifth edition, international student edition, 2020. ISBN 978-1-260-54788-7.
- [25] J. K. Black. Nonlinear behavior of additively manufactured steel beams with trapped-powder dampers: Supplementary Files. August 2025. doi:10.5281/zenodo.15001945.
- [26] T. Zhang and L. Yuan. Understanding surface roughness on vertical surfaces of 316 L stainless steel in laser powder bed fusion additive manufacturing. *Powder Technology*, 411:117957, October 2022. ISSN 00325910. doi:10.1016/j.powtec.2022.117957.
- [27] Z. Xiang, M. Yin, Z. Deng, X. Mei, and G. Yin. Simulation of Forming Process of Powder Bed for Additive Manufacturing. *Journal of Manufacturing Science and Engineering*, 138(8):081002, August 2016. ISSN 1087-1357, 1528-8935. doi:10.1115/1.4032970.
- [28] O. Barrau, C. Boher, C. Vergne, F. Rezai-Aria, and R. Gras. Investigations of Friction and Wear Mechanisms of Hot Forging Tool Steels. Karlstad University, 2002. Karlstad University, URL https://www5.kau.se/sites/default/files/Dokument/subpage/2010/02/8_95_111_pdf_58241.pdf.
- [29] B. Rehmer, F. Bayram, L. A. Ávila Calderón, G. Mohr, and B. Skrotzki. BAM reference data: Temperature-dependent Young's and shear modulus data for additively and conventionally manufactured variants of austenitic stainless steel AISI 316L. January 2025. doi:10.5281/ZENODO.14616480.
- [30] 3M. 3M[™] Viscoelastic Damping Polymer 112 Series, May 2017, URL https://multimedia.3m.com/mws/media/8281340/3m-viscoelastic-damping-polymer-112-series.pdf.